CPM-based Tunable Phase-Attached Radar-Communications (PARC)

Cenk Sahin[1], Patrick M. McCormick[2], Justin G. Metcalf[3],
John Jakabosky[4], Shannon D. Blunt[2], Erik S. Perrins[2], and Jonathan Owen[2]
[1] Johns Hopkins University Applied Physics Laboratory, Laurel, MD
[2] Department of Electrical Engineering & Computer Science, University of Kansas, Lawrence, KS
[3] Advanced Radar Research Center, University of Oklahoma, Norman, OK
[4] Radar Division, Naval Research Laboratory, Washington, DC

***Abstract*—Motivated by the increasing need for efficient use of the electromagnetic spectrum in congested and contested environments, a co-designed dual-function radar-communications waveform framework was introduced that combines the desirable features of a pulsed radar transmission (i.e., constant amplitude and continuous phase) with the ability to embed information in the phase of the waveform via continuous phase modulation (CPM). This CPM-based phase-attached radar-communications (PARC) waveform operates in a pulse-agile mode, which introduces a coupling of the fast- and slow-time dimensions through what is known as range-sidelobe modulation (RSM). The flexibility of CPM-based PARC via its multiple tunable parameters provides the ability to control this radar performance degradation at the expense of bit error rate and/or data throughput. Furthermore, the severity of RSM can likewise be mitigated via mismatched filter pulse compression on receive to reduce the variance of the pulse compression responses. Here, we evaluate the radar and communications performance trade-space as a function of the CPM-based PARC parameters when assuming both matched and mismatched filter pulse compression at the radar receiver. The efficacy of the CPM-based PARC framework for both radar and communications is experimentally validated in an open-air environment using a radar in a quasi-monostatic configuration and a communication receiver in the field-of-view of the radar.**

***Index Terms*—Dual-function radar-communications (DFRC), mismatched filtering, spectrum sharing, radar-communications co-design**

I. Introduction

The electromagnetic spectrum (EMS) is a fixed resource with an exponentially increasing demand from commercial communication applications [1]–[3]. The resulting erosion of radar spectrum to meet this communication demand is creating additional strain on defense applications that must already operate in congested and contested environments. As such, ongoing research is focused on improving spectral efficiency [3], [4] or developing methods to share spectrum between multiple functions (e.g. radar and communication sharing spectrum [5]–[16]).

Generally speaking, spectrum sharing can take two forms: cohabitation or co-design. Where the former tends primarily to address the interference that separately operated systems could cause to one another, the latter involves cooperative control within the same system. Here, we investigate the co-design problem, in particular the realization of a single dual-function system with both radar and communication capabilities. This dual-function radar-communications (DFRC) framework provides a means to improve spectral efficiency by performing multiple functions within the same transmission [17], [18]. While communications and radar functions both use the EMS, they have competing constraints. Communications waveforms maximize information throughput by maximizing the entropy of the waveform [19]. In contrast, radar waveforms require coherent, restrictive forms to maximize detection performance (i.e., sidelobe performance, receive processing complexity, etc.) [20]. Therefore, a dual-function system that performs radar and communication simultaneously necessarily involves a performance trade-off between these functions.

Aside from the more obvious approaches of time-sharing or frequency sub-banding, the notion of radar-communication spectrum sharing necessitates the use of some manner of waveform diversity [21]–[25]. As a general principle, waveform diversity can involve the exploitation of the available time, frequency, coding, spatial, and/or polarization degrees-of-freedom. For example, other work has examined using a small set of distinct radar waveforms where each represents a different communication symbol [26], [27], modulating a communication signal onto the spatial sidelobes of a radar beam [28], using 4G communication signals to also serve as short-range radar emissions for automotive applications [29], tandem hopping of communications within spectral gaps of the radar emission [30], and phase-modulating a linear FM (LFM) waveform [31]–[33]. The latter formulation is particularly relevant for the proposed approach.

In general, co-design has become synonymous with the field of integrated sensing and communications (ISAC), a fast moving research area with strong interest from the commercial sector [34]. However, the present work considers a different set of constraints than is typical in the current literature. Specifically, the radar is assumed to be operating in a long-

Portions of this research were performed while Cenk Sahin held an NRC Research Associateship award at the Sensors Directorate, Air Force Research Laboratory and Justin G. Metcalf was with the Sensors Directorate, Air Force Research Laboratory, and was previously published in [40], [41], [43]. The work was supported in part by the Naval Research Laboratory - Radar Division, the Air Force Research Laboratory - Sensors Directorate, a subcontract with Matrix Research, Inc. for research sponsored by Air Force Research Laboratory under Prime Contract #FA8650-14-D-1722, and the Office of Naval Research under contract #N00014-23-C-1053. DISTRIBUTION STATEMENT A. Approved for public release.

range surveillance mode with a high clutter background. These two practical attributes greatly restrict the design of the waveform. For instance, the long-range requirement effectively forces the waveform to be constant modulus and spectrally well-contained to address the rigors of a high-power transmitter. Further, to ensure maximum energy-on-target, the communication capability should avoid deviation from the spatial distribution of energy (i.e., beampattern) required during normal radar operations and must only be incorporated via the waveform modulation. For cross-compatibility with existing devices, the communications protocol chosen should also minimally deviate from standard waveforms. This last design goal restricts the ability to jointly optimize radar and communications waveforms as the communication signaling scheme should be drawn from an existing family with well-characterized demodulation schemes and performance curves. Consequently, a heuristic approach is chosen for the joint radar-communications waveform design, leveraging classical power- and spectrum-efficient design techniques.

As is the case with most radar applications, some communication systems require spectrally contained signals with good power efficiency (e.g. aeronautical telemetry [35]). To meet this need, a family of constant-envelope signaling schemes was developed, collectively denoted as continuous phase modulation (CPM) [36]. The continuous-phase feature of CPM signals leads to good spectral efficiency while the constant-envelope feature translates to robustness against the distortion introduced by nonlinear components in the transmitter (e.g. the power amplifier). As a result, the transmitter power amplifier can be operated in saturation such that the available power is efficiently converted into radiated power. Due to these favorable features, CPM is used in the Bluetooth wireless standard [37] and two variants of shaped-offset quadrature phase-shift keying (SOQPSK) modulation, a type of CPM, are standardized for military applications (SOQPSK-MIL) [38] and aeronautical telemetry (SOQPSK-TG) [35].

The notion of pulse agility (or waveform agility), in which the radar waveform is allowed to change on a pulse-to-pulse basis, was examined in [26] as a means to incorporate a communication function into the radar emission, where the set of possible waveforms serves as a communication symbol alphabet. The primary issue with varying the radar waveform during a coherent processing interval (CPI) is the clutter *range sidelobe modulation* (RSM) [26], [39], [40] that arises because the pulse compression of different waveforms leads to different sidelobe structures. When Doppler processing is carried out across the CPI of pulsed echoes, the presence of RSM induces a partial loss of coherency in range sidelobes and spread of energy across the entire Doppler space thus degrading target visibility. In [26], filter design to mitigate RSM for a given set of waveforms was addressed via the development of the iterative joint least squares (JLS) algorithm. However, JLS is only suitable for transmitting $1-2$ bits per pulse because the performance diminishes as the number of waveforms increases. In [27] a closed-form solution is derived for the JLS approach for moving target indication (MTI) radar, though the new form is likewise only applicable to low data rates.

Here, we introduce and evaluate a co-designed radar-communications waveform model whereby information-bearing sequences are modulated with CPM and *phase-attached* to a *fixed* radar waveform (e.g., an LFM) that remains constant over a coherent processing interval [41]. This CPM-based phase-attached radar-communications (PARC) waveform is both constant-envelope and continuous-phase to ensure a spectrally efficient transmission amenable to high power (saturated) amplification. Phase-modulating an LFM waveform as a means of embedding communications into radar was proposed in [32], [33]. Specifically, in [32] information sequences modulated with MSK are multiplied by an LFM pulse while in [33] information sequences modulated with phase-shift keying (PSK) [42] having an adjustable phase parameter are multiplied by a higher rate pseudorandom binary sequence (i.e. spread spectrum) and then a discretized LFM pulse. The CPM-based PARC waveform model described here is a generalization that provides more control over the trade-space between radar and communications performance via multiple tunable parameters.

While the random nature of the embedded communications produces a pulse-agile transmission, the adjustable communications parameters of CPM-based PARC provide control of the severity of RSM by trading off bit error rate (BER) and/or data throughput. Here, we evaluate the radar and communications performance trade-space as a function of the embedded communications parameters. Under the assumption of homogeneous clutter statistics, we introduce an expression for predicting the severity of RSM due to clutter called clutter RSM (C-RSM) power as a function of the PARC waveform parameters and method of fast-time (pulse compression) and slow-time (Doppler compression) processing. Furthermore, we show that the radar-communications trade-space can be more advantageous for each function via mismatched filtering on receive to mitigate RSM without sacrificing communications performance [43], [44]. Finally, CPM-based PARC was experimentally validated in an open-air environment using a quasi-monostatic radar configuration and communications receiver. The main contributions of the paper are as follows:

- Characterization of the spectral content of PARC waveforms for various communications parameters, and mitigation of spectral spreading via guard symbols.
- Characterization of radar and communications performance trade-offs as a function of the PARC parameters via bit-error rate and point spread function analysis.
- Derivation of the zero-Doppler clutter power spectral density for a set of PARC pulses and the expected C-RSM level.
- Characterization of C-RSM mitigation via mismatched filter design according to a desired template.
- Open-air demonstration of the PARC concept using quasi-monostatic radar and communications receiver.

The organization of the paper is as follows: Section II introduces the CPM-based PARC signal model and evaluates the effect of attached communications on the waveform energy spectral density (ESD), Section III evaluates the PARC system performance (both communications and radar) as a function of the selection of waveform parameters, Section IV introduces a method of computing the expected C-RSM power for a set of PARC parameters, and demonstrates the ability of mismatched filtering to mitigate C-RSM, and Section V describes the experimental evaluation of CPM-based PARC in both a radar and communications context.

II. CPM-Based Tunable PARC

The CPM-based PARC framework is a co-designed DFRC technique using coding diversity, where the emission embeds unique information on a pulse-to-pulse basis using a specific waveform modulator, thereby creating a pulse-agile transmission [26], [27], [32], [33], [41], [45]. Each unique waveform is associated with a distinct information sequence; however, all waveforms have the same time duration and spectral support to ensure coherence of the radar backscatter from pulse-to-pulse. The emission is captured by a communications receiver within the illuminated scene that estimates the embedded information sequence. In this work, only the "downlink" path (from radar system to communications receiver) is considered.

Figure 1 illustrates the system concept of a CPM-based PARC implementation comprised of monostatic radar system with information-embedded PARC waveforms and a communications user that receives the embedded information. The radar system consists of a CPM modulator (to embed the information sequence) and mismatched filter (or matched filter) generation stage to form filters for pulse compression. While the analysis in this work is extensible to other radar modes (e.g., synthetic aperture radar [44]), here we focus on a pulse-Doppler radar product. The communications receiver consists of a synchronization block, radar phase function removal, and estimation of the symbol sequence via the Viterbi algorithm [36]. Note that for dispersive communications channels, an equalization stage would likewise need to be implemented (analysis of equalization for PARC transmissions is left for future work).

The PARC concept is an alternative to using a pure CPM waveform (i.e., no base radar waveform) to perform both communications and radar functions. While a CPM waveform would provide the best communications performance (i.e., throughput), the radar performance (i.e., range sidelobe and RSM levels) will be dictated by the time-bandwidth product of the CPM pulse and the number of integrated pulses which may not be desirable for all applications (see [46] for a discussion on this topic for random frequency modulated waveforms). Modulation of the CPM onto a base radar waveform decouples the overall pulse bandwidth and RSM performance allowing for tunability of the radar and communications performance via the CPM parameters.

A. PARC Signal Model

The PARC waveform of pulse duration T transmitted during the n_{p}-th pulse repetition interval (PRI) in an N_{p}-pulse CPI is modeled as [41]

$$s(t;\boldsymbol{\alpha}_{n_{\mathrm{p}}}) = \begin{cases} e^{j(\psi(t)+\phi(t;\boldsymbol{\alpha}_{n_{\mathrm{p}}}))} & 0 \le t < T \\ 0 & \text{otherwise} \end{cases}, \tag{1}$$

where $\psi(t)$ is the phase function of the fixed base radar waveform, and $\phi(t;\boldsymbol{\alpha}_{n_{\mathrm{p}}})$ is the communications phase function modulated by length-N_{s} symbol sequence $\boldsymbol{\alpha}_{n_{\mathrm{p}}} = [\alpha_{n_{\mathrm{p}},0}, \cdots, \alpha_{n_{\mathrm{p}},N_{\mathrm{s}}-1}]$ where $\alpha_{n_{\mathrm{p}},n_{\mathrm{s}}}$ is the n_{s}-th symbol of the n_{p}-th pulse. Here, the fixed radar phase function follows the up-chirped LFM structure,

$$\psi(t) = 2\pi\left(-\tfrac{B}{2}t + \tfrac{B}{2T}t^2\right), \tag{2}$$

for swept bandwidth B; however, any fixed signal structure can be implemented in the PARC framework (e.g., nonlinear LFM [47]). The communications phase function $\phi(t;\boldsymbol{\alpha}_{n_{\mathrm{p}}})$ is modulated via CPM as [36]

$$\phi(t;\boldsymbol{\alpha}_{n_{\mathrm{p}}}) = h\pi\int_0^t \left[\sum_{n_{\mathrm{s}}=0}^{N_{\mathrm{s}}-1} \alpha_{n_{\mathrm{p}},n_{\mathrm{s}}}\, q(\eta - n_{\mathrm{s}}T_{\mathrm{s}})\right] d\eta, \tag{3}$$

where h is the modulation index, $q(t)$ is the shaping filter, $T_{\mathrm{s}} = \frac{T}{N_{\mathrm{s}}}$ is the symbol period, and each symbol is drawn from the M-ary alphabet $\alpha_{n_{\mathrm{p}},n_{\mathrm{s}}} \in \{\pm1, \pm3, \cdots, \pm(M-1)\}$ where M is the size of the alphabet. The shaping filter $q(t)$ has time duration LT_{s} with L a positive integer, and integrates to unity. When $L = 1$ the CPM waveform is said to be *full-response*; otherwise (i.e., $L > 1$), it is *partial-response*. Partial-response CPM generally results in superior spectral containment at the expense of increased communication receiver complexity [36], [42]. The communication symbol sequence $\boldsymbol{\alpha}_{n_{\mathrm{p}}}$ is obtained from the length-N_b binary information sequence $\mathbf{b}_{n_{\mathrm{p}}}$ where $N_b = mN_{\mathrm{s}}$ and $m = \log_2 M$ (number of bits per symbol) is called the modulation order.

Given the phase functions in (2) and (3), the CPM-PARC waveform is constant envelope and continuous phase. The continuous-phase property leads to high spectral efficiency and provides a compact spectral roll-off, thereby ensuring good spectral containment. The constant-envelope attribute allows the radar transmitter power amplifier to be operated in saturation, which maximizes the transmit power and corresponding "energy on target."

The PARC waveform model in (1) can also be viewed as the time-domain product between the deterministic radar waveform $e^{j\psi(t)}$ and a stochastic communication waveform $e^{j\phi(t;\boldsymbol{\alpha}_{n_{\mathrm{p}}})}$ modulated by the information sequence $\boldsymbol{\alpha}_{n_{\mathrm{p}}}$. The base radar waveform maintains a degree of commonality across the set of changing PARC waveforms in the CPI that is uniquely specified by the tunable parameters h, m, and T_{s}, with greater commonality translating to reduced RSM [40]. These parameters also specify the communication performance, (i.e., BER and data throughput), and therefore establish a trade-space where the radar performance can be improved by accepting a reduced communication performance, and vice versa. In Section IV, we show that mismatched filtering can largely mitigate this performance degradation by matching the pulse compression output to a common response over all pulses.

Other PARC approaches in the literature involve the phase modulation of an LFM radar waveform [32], [33]. In [32], information sequences modulated with minimum-shift keying (MSK) are multiplied by an LFM pulse. In [33], information sequences modulated with PSK [42] having an adjustable phase parameter are multiplied by a higher rate pseudorandom binary sequence (i.e., spread spectrum) and then a discretized

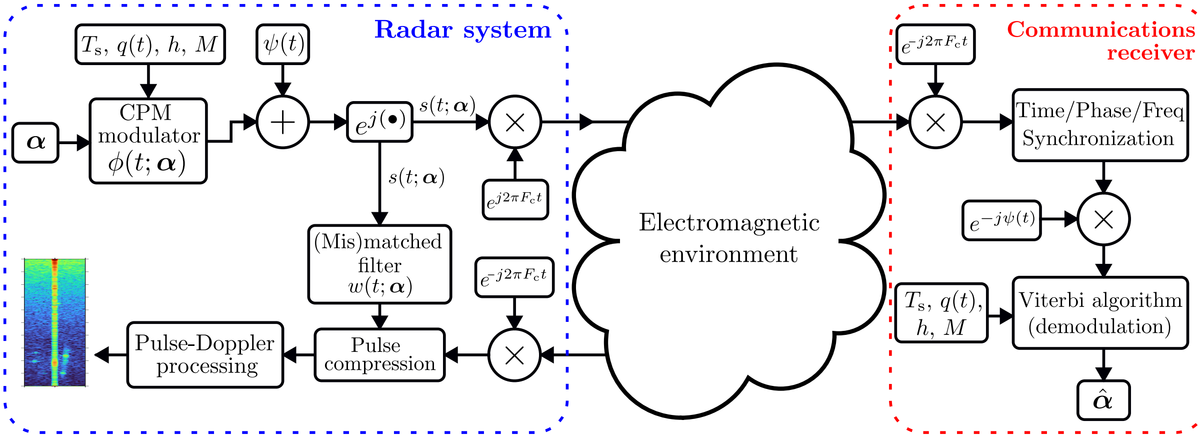

Fig. 1. System concept of a CPM-based PARC implementation including monostatic radar system with CPM modulator and communications receiver.

LFM pulse. The CPM-PARC scheme presented here represents a generalization of such approaches, the spreading of [33] notwithstanding, that is applicable to arbitrary FM radar waveforms (e.g., linear and non-linear FM). Specifically, MSK can be modeled as a special case of binary CPM. Likewise, PSK with an adjustable phase parameter can be implemented as a CPM waveform with an adjustable modulation index, an impulse function $\delta(\tau)$ as the shaping filter, and a precoder to convert binary PSK symbols to ternary CPM symbols akin to the CPM implementation of shaped-offset quadrature PSK (SOQPSK) [35], [38], [48]. The generalization of the waveform model via the CPM framework with parameters (i.e., h, T_s, M, and $q(t)$) allows for finer control over the radar and communications trade-space.

B. Spectral Content

The modulation index h, a rational number, is a key parameter as it controls the total phase change over of communication symbol interval T_s. For rectangular $q(t)$ with $L=1$, the phase change due to α_{n_p,n_s} over a symbol period is $h\pi\alpha_{n_p,n_s}$, such that the magnitude of the maximum phase change is $h\pi(M-1)$. Therefore, when $\phi(t;\boldsymbol{\alpha}_{n_p})$ is added to $\psi(t)$, this additional phase deflection results in a spectral broadening relative to the base radar waveform $e^{j\psi(t)}$. This broadening effect can also be observed from (1) by noting that the Fourier transform of $s(t;\boldsymbol{\alpha}_{n_p})$ is the convolution of the Fourier transforms of $e^{j\psi(t)}$ and $e^{j\phi(t;\boldsymbol{\alpha}_{n_p})}$, resulting in a wider spectral response on average.

To quantify the expected spectral content of the PARC waveform, we must consider (for fixed CPM-PARC parameters) the entire set of possible CPM-PARC waveforms $s(t;\tilde{\boldsymbol{\alpha}}_k)$ for $k=0,\cdots,2^{N_b}-1$, where $\tilde{\boldsymbol{\alpha}}_k$ describes the entire set of possible symbol sequences. Since PARC is a pulsed signal (finite energy), the spectral content is defined as the expected energy spectral density (ESD),

$$P_s(f)=\mathcal{E}_{\tilde{\boldsymbol{\alpha}}_k}\{|S(f;\tilde{\boldsymbol{\alpha}}_k)|^2\}, \tag{4}$$

where $\mathcal{E}_{\tilde{\boldsymbol{\alpha}}_k}\{\bullet\}$ is the expectation over the set of possible symbol sequences, and

$$S(f;\tilde{\boldsymbol{\alpha}}_k)=\int_0^T s(t;\tilde{\boldsymbol{\alpha}}_k)e^{-j2\pi ft}dt \tag{5}$$

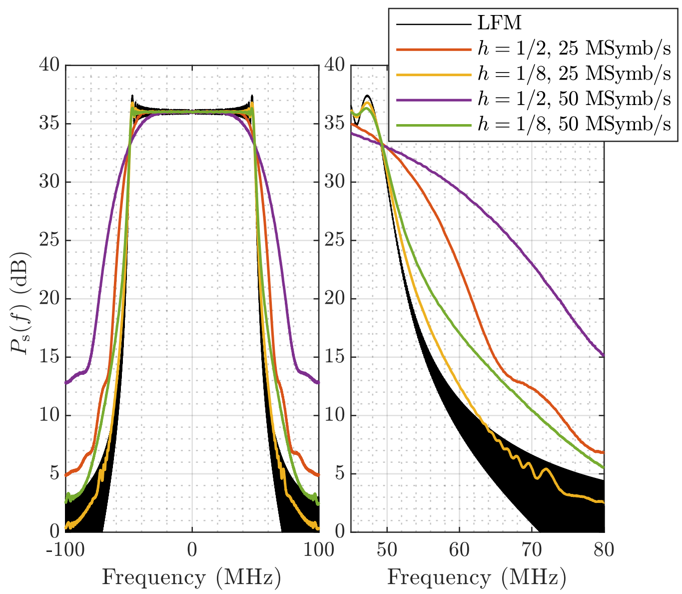

Fig. 2. Expected ESD $P_s(f)$ of PARC waveforms (from (4)) with LFM bandwidth $B=100$ MHz and pulsewidth $T=10$ μs (ESD shown in black) and four different binary ($M=2$) CPM sequences with rectangular shaping filter $q(t)$: $h=\frac{1}{2}$ and $F_s=25$ MSymb/s (red), $h=\frac{1}{8}$ and $F_s=25$ MSymb/s (yellow), $h=\frac{1}{2}$ and $F_s=50$ MSymb/s (purple), and $h=\frac{1}{8}$ and $F_s=50$ MSymb/s (green).

is the Fourier transform of the PARC waveform. The severity of spectral broadening in the expected ESD of the PARC waveform relative to the ESD of the base radar waveform $e^{j\psi(t)}$ is dependent on the spectral content of the information-bearing CPM signal, $e^{j\phi(t;\tilde{\boldsymbol{\alpha}}_k)}$. All communications parameters (i.e., modulation index h, modulation order m, symbol period T_s, and shaping filter $q(t)$) influence the CPM spectral content.

For example, consider an LFM base radar waveform with $B=100$ MHz and $T=10$ μs, and an attached binary ($M=2$) CPM sequence for the following parameter pairs: modulation indices $h=\frac{1}{2}$ and $h=\frac{1}{8}$, symbol rates $F_s=\frac{1}{T_s}=25$ and $F_s=50$ MSymb/s, and rectangular ($L=1$) and raised-cosine ($L=3$) shaping filters $q(t)$. The

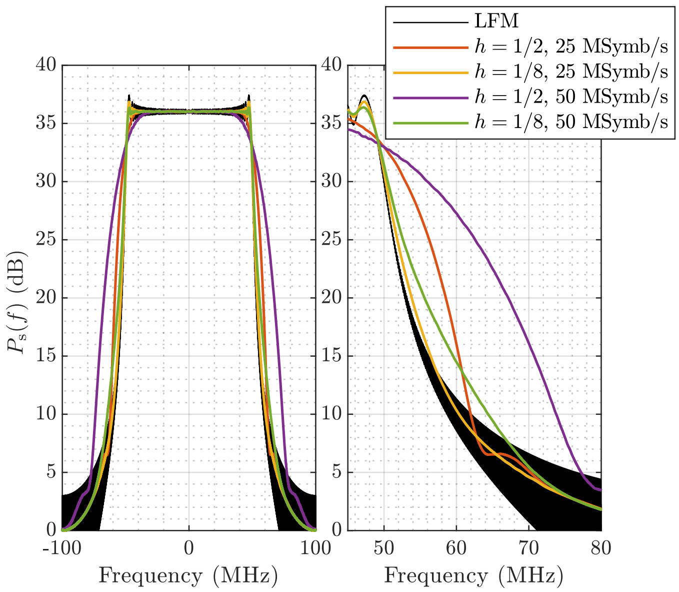

Fig. 3. Expected ESD $P_s(f)$ of PARC waveforms (from (4)) with LFM bandwidth $B = 100$ MHz and pulsewidth $T = 10$ μs (ESD shown in black), and four different binary ($M = 2$) CPM sequences with raised-cosine shaping filter $q(t)$: $h = \frac{1}{2}$ and $F_s = 25$ MSymb/s (red), $h = \frac{1}{8}$ and $F_s = 25$ MSymb/s (yellow), $h = \frac{1}{2}$ and $F_s = 50$ MSymb/s (purple), and $h = \frac{1}{8}$ and $F_s = 50$ MSymb/s (green).

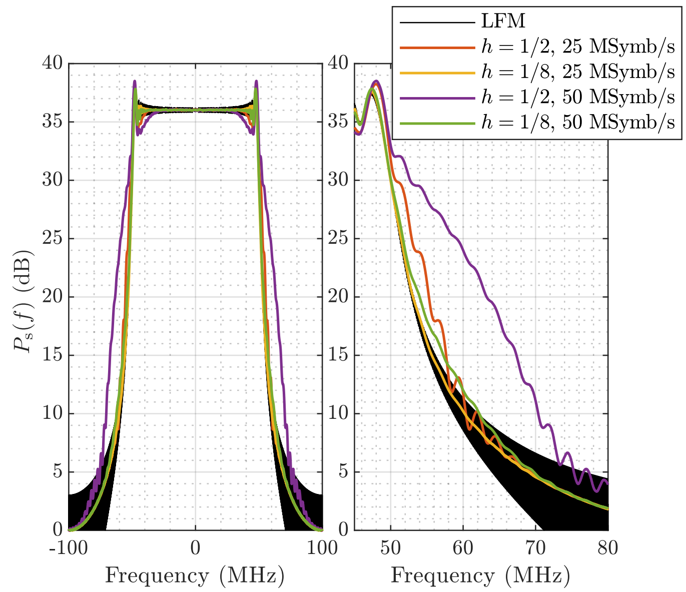

Fig. 4. Expected ESD $P_s(f)$ of PARC waveforms (from (4)) with LFM bandwidth $B = 100$ MHz and pulsewidth $T = 10$ μs (ESD shown in black), and four different binary ($M = 2$) CPM sequences with $L = 3$ raised-cosine shaping filter $q(t)$: $h = \frac{1}{2}$, $N_g = 8$, and $F_s = 25$ MSymb/s (red); $h = \frac{1}{8}$, $N_g = 8$ guard symbols, and $F_s = 25$ MSymb/s (yellow); $h = \frac{1}{2}$, $N_g = 18$ guard symbols, and $F_s = 50$ MSymb/s (purple); and $h = \frac{1}{8}$, $N_g = 18$ guard symbols, and $F_s = 50$ MSymb/s (green).

shaping filters are expressed as

$$q(t) = \begin{cases} 1/T_s & 0 \le t < T_s \\ 0 & \text{otherwise} \end{cases} \tag{6}$$

for the rectangular shaping filter, and

$$q(t) = \begin{cases} \frac{1}{LT_s}\left(1 - \cos(2\pi \frac{t}{LT_s})\right) & 0 \le t < LT_s \\ 0 & \text{otherwise} \end{cases} \tag{7}$$

for the raised-cosine shaping filter. Figure 2 shows $P_s(f)$ from (23) for the rectangular shaping filter case compared to the ESD of the base radar waveform, while Fig. 3 shows $P_s(f)$ using the raised-cosine shaping filter for $L = 3$. We observe in these figures that the bandwidth of PARC waveforms increases with increasing h and F_s [42], and the spectral roll-off of the $P_s(f)$ is dependent on the communication shaping filter $q(t)$, with the longer and smoother raised-cosine shaping filter translating to less broadening.

Note that while the communications parameters can be tuned to control the expected ESD of the PARC waveform, the communications performance and/or demodulation receiver complexity likewise changes [42]. As an alternative to altering the CPM parameters, the spectral broadening can also be controlled via *guard symbols* at the beginning and end of the pulse for particular waveform types. Specifically, for chirp-like radar waveforms (e.g., LFM and most nonlinear FM) that traverse the band during the pulse, the extrema of the frequency content occur at the beginning and end of the pulse; therefore, if the waveform is not modulated for communications during this time, the spectral broadening can be significantly mitigated in exchange for a small reduction in throughput. This arrangement is equivalent to transmitting *null* CPM communication symbols at the beginning and end of the pulse, $\alpha_{n_p,n_s} = 0$ for $0 \le n_s \le N_g - 1$ and $n_s - N_g \le n_s \le N_s - 1$, for some number of guard symbols N_g resulting in a *guard time* of $T_g = N_g T_s$. Figure 4 shows the raised-cosine shaping filter case from Fig. 3 with $N_g = 8$ guard symbols ($T_g = 0.32$ μs) for the $F_s = 25$ MSymb/s cases and $N_g = 18$ guard symbols ($T_g = 0.36$ μs) for the $F_s = 50$ MSymb/s cases. By adding these guard symbols at the beginning and end of the pulse, all cases (except the $h = \frac{1}{2}$ and $F_s = 50$ MSymb/s case) now have comparable spectral roll-offs to the base LFM ESD.

III. PARC System Performance

In this section, we discuss in detail the radar performance and the communication performance of the CPM-based PARC as a function of its tunable parameters. The communications performance is dictated by bit error rate (BER) while radar performance is evaluated via notional point target range-Doppler responses (i.e., point spread functions). These measures illustrate the inherent trade-off between radar and communications performance when implementing a matched filter radar receiver.

A. Communication Performance

Assuming a single strong propagation path between the radar transmitter and the communication receiver, the baseband received signal at the communication receiver (after down-conversion) can be expressed as

$$y_c(t; \boldsymbol{\alpha}_{n_p}) = \sqrt{P_r}\, s(t - \tau_r; \boldsymbol{\alpha}_{n_p}) e^{j2\pi F_r (t-\tau_r)} e^{j\theta_r} + u(t), \tag{8}$$

where P_r is the received power, τ_r, F_r, and θ_r are the delay, frequency, and phase offsets between the radar system and communications receiver, respectively, and $u(t)$ is a zero-mean circularly symmetric complex-valued Gaussian noise process with flat power spectral density (PSD) N_0. Since only a single dominant path is assumed, synchronization of the received signal is performed via estimation and removal of offsets τ_r, F_r, and θ_r [49]. More complicated channels with delay and/or Doppler dispersive properties will require channel estimation and equalization methods to correct for frequency selective channels [42].

Synchronization of $y_\mathrm{c}(t;\boldsymbol{\alpha}_{n_\mathrm{p}})$ is performed by estimation of τ_r and θ_r for time and phase alignment, and removal of the base radar waveform phase function via a product with its conjugate $e^{-j\psi(t)}$. The synchronized baseband receive signal then takes the form

$$\begin{aligned}\tilde{y}_\mathrm{c}(0 \le t < T;\boldsymbol{\alpha}_{n_\mathrm{p}}) &= e^{-j\psi(t)} y(t+\tau_\mathrm{r};\boldsymbol{\alpha}_{n_\mathrm{p}}) e^{-j2\pi F_\mathrm{r} t} e^{-j\theta_\mathrm{r}} \\ &= \sqrt{P_\mathrm{r}} e^{j\phi(t;\boldsymbol{\alpha}_{n_\mathrm{p}})} + \tilde{u}(t)\end{aligned}, \tag{9}$$

where $\tilde{u}(t) = e^{-j\psi(t)} u(t+\tau_\mathrm{r}) e^{-j2\pi F_\mathrm{r} t} e^{-j\theta_\mathrm{r}}$ is the resulting noise process, which is statistically equivalent to $u(t)$ over $0 \le t < T$ due to stationarity, flat PSD, and circular symmetry of its statistics. Under ideal synchronization, $\tilde{y}_\mathrm{c}(t;\boldsymbol{\alpha}_{n_p})$ only depends on the communication sequence $\boldsymbol{\alpha}_{n_p}$; therefore, the BER does not depend on the radar parameters. The optimal detection of $\boldsymbol{\alpha}_{n_p}$, which requires maximum likelihood sequence detection, then can be achieved by applying the Viterbi algorithm [50]. The Viterbi algorithm operates on a trellis with pM^{L-1} states representing the CPM scheme [42]. As stated previously, the modulation index is a rational number (i.e., $h = \frac{u}{v}$ with positive integers u, v), M is the size of the alphabet, and L is a positive integer specifying the shaping filter duration LT_s [42]. The value of p is equal to $2v$ when u is an even number, and p is equal to v when u is odd [42].

Note that complete removal of the base radar waveform at the communication receiver (as in (9)) requires perfect timing estimation. Timing estimation errors at the communication receiver will lead to residual phase errors after synchronization and degrade communication performance (i.e., increase BER) due to CPM being a type of phase modulation. To give an example, with time-frequency coupled base radar waveforms (e.g., LFM) timing errors translate to frequency offset errors in the communication signal due to the multiplication of the received PARC waveform by the complex conjugate of the base radar waveform. The resulting frequency offset will lead to a linear phase error across the pulse. With coherent demodulation of CPM waveforms using small modulation indices even small phase errors significantly can degrade communication performance. Likewise, any mismatch, especially phase mismatch, between the waveform used for base radar waveform removal and the received signal radar waveform component will lead to communication performance degradation. In this work we assume perfect synchronization, and the impact of imperfect synchronization on communications performance will be examined in future works.

Because of the memory of CPM waveforms, exact closed-form BER expressions are in general not available. In addition, for a given received power P_r and noise PSD N_0, the BER depends on all CPM parameters: h, M, T_s, and $q(t)$. Here, we focus on full-response CPM with a rectangular shaping filter with $L = 1$ (full-response), for which accurate BER approximations are available, and discuss the relationship between the BER and CPM parameters h, M, and T_s. CPM with a full-response rectangular shaping filter is also known in the literature as continuous-phase frequency-shift keying (CPFSK [42]). Also note that with the CPM-PARC approach, the radar transmit power does not vary with alphabet size M. It follows that when comparing the BER rates for different values of M, the symbol energy $E_\mathrm{s} = T_\mathrm{s} P_\mathrm{r}$—rather than bit energy—is kept constant.

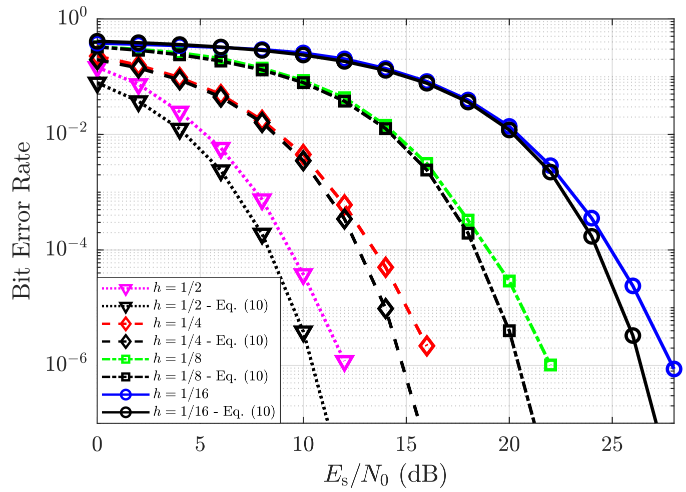

Fig. 5. The bit error rate (BER) of binary ($M = 2$) CPM with $L = 1$ rectangular shaping filter $q(t)$ for various modulation indices h and approximate BER curves using (10) with $K_M = 1$.

The symbol error rate (SER) of full-response CPM with a rectangular shaping filter can be approximated by [42]

$$\mathrm{SER}(h, T_\mathrm{s}, M, P_\mathrm{r}, N_0) \approx K_M\, Q\left(\sqrt{\frac{T_\mathrm{s} P_\mathrm{r}}{N_0} 2\left(1 - \frac{\sin 2h\pi}{2h\pi}\right)}\right) \tag{10}$$

and $h \le \frac{1}{2}$, where $K_M \ge 1$—the average number of minimum-distance paths—is some constant depending on M, and $Q(x) = \int_x^\infty \frac{1}{\sqrt{2\pi}} e^{-\frac{\eta^2}{2}} d\eta$. For the binary case ($M = 2$), the BER is equal to the SER, while for higher order modulations it is bounded as $\mathrm{SER}/m < \mathrm{BER} < \mathrm{SER}$. We verified by simulation that this approximation is very accurate for modulation indices $h = \frac{1}{4}$ and below with $M = 2$, $M = 4$, and $M = 8$ using $K_M = 1$, $K_M = 2.25$, and $K_M = 3.25$, respectively. We refer to the argument of the square root inside the Q function as the *effective communication SNR*, or simply the effective SNR. Because the CPM phase function has memory, CPM waveforms are assumed to be infinitely long for analytical purposes. The SER expression (10) is derived under this assumption. In reality, CPM waveforms have finite durations and the symbols in the beginning and end of CPM waveforms may be subject to higher SERs than those in the middle.

When h is small, the effective SNR decreases approximately by a factor of 4 if h is divided by 2 (a 6 dB

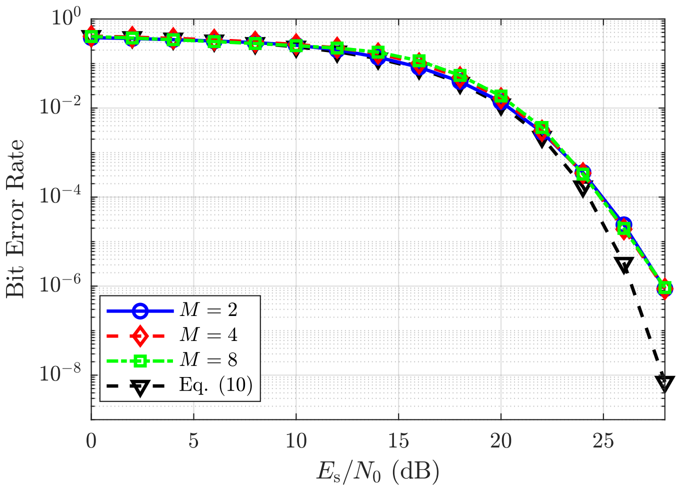

Fig. 6. The bit error rate (BER) of CPM with $L = 1$ rectangular shaping filter and $h = \frac{1}{16}$ for various values of the modulation order $m = \log_2 M$ and the BER curve using (10) with $K_M = 1$ for the binary case ($M = 2$).

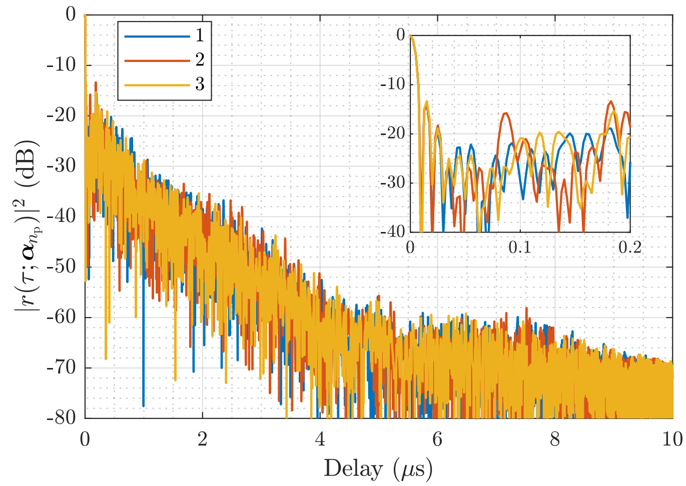

Fig. 7. Demonstration of RSM via autocorrelation responses $|r(\tau; \boldsymbol{\alpha}_{n_\mathrm{p}})|^2$ (dB) of three randomly generated PARC waveforms with LFM bandwidth of $B = 100$ MHz and pulsewidth $T = 10$ μs, and binary ($M = 2$) CPM with $h = \frac{1}{8}$, $F_\mathrm{s} = 50$ MSymb/s, $L = 1$ rectangular shaping filter, and no guard symbols.

loss). This can be shown using the trigonometric identity $\sin 2h\pi = 2 \sin h\pi \cos h\pi$, invoking a two-term Taylor series expansion around 0 as $\sin h\pi \approx (h\pi - (h\pi)^3/6)$ and $\cos h\pi \approx 1 - (h\pi)^2/2$, and then singling out the dominant terms. It follows from a communication performance perspective that it is desirable to increase h. Per (10), increasing T_s (or decreasing F_s) increases the effective SNR, and hence reduces the SER and BER. However, increasing T_s also reduces the data throughput as it decreases the number of data symbols per pulse N_s. The effective SNR does not vary with M. Increasing M increases K_M and decreases the BER lower bound in terms of the SER. As such, the BER does not significantly vary with M. On the other hand, the data throughput, given as mN_s bits per pulse, increases with M.

As an example, consider the BER resulting from the use of binary CPM with a full-response rectangular shaping filter (i.e., binary CPFSK) and $N_\mathrm{s} = 64$ symbols/pulse as a function of communication receiver SNR (i.e., $\frac{E_\mathrm{s}}{N_0} = \frac{T_\mathrm{s} P_\mathrm{r}}{N_0}$) for modulation indices $h = \frac{1}{2}, \frac{1}{4}, \frac{1}{8}$, and $\frac{1}{16}$. The resulting BER curves and their approximations using (10) with $K_M = 1$ are shown in Fig. 5, where it is observed that the required SNR to achieve a given BER increases with decreasing modulation index h. In particular, the SNR gap between the $h = \frac{1}{16}$ and $h = \frac{1}{8}$ curves is 6 dB, which is consistent with the analysis above. For $h = \frac{1}{4}, \frac{1}{8}$, and $\frac{1}{16}$, the BER curves obtained with (10) slightly underestimate the BER than those obtained by simulation which uses finite-block (64 symbol) CPM waveforms.

Figure 6 shows the BER curves for modulation order values $m = 1, 2,$ and 3 (or $M = 2, 4,$ and 8) and the BER curve from (10) using $K_M = 1$ for the binary case ($M = 2$). The modulation index is $h = \frac{1}{16}$ and all other parameter values are the same as those used for Fig. 5. It is observed that the BER remains approximately constant as a function of m (or M) as the SNR (i.e., $\frac{E_\mathrm{s}}{N_0}$) is varied from 0 dB to 28 dB. Note, however, that an increase in M alone will likewise increase the communications bandwidth. Similar to Fig. 5, the BER curve obtained with (10) matches BER curves obtained by simulation below 22 dB, while it leads to a lower BER above 22 dB due the simulation having finite-block CPM waveforms.

B. Radar Performance

The correlation performance of the PARC radar receiver is highly dependent on the selection of the CPM parameters. The stochastic nature of PARC (via the embedding of information) makes it a *pulse agile* emission, where the modulation of the waveform changes on a pulse-by-pulse basis. The autocorrelation function of a waveform provides the single pulse, point target response under a matched filter processing assumption, and provides a means of evaluating radar performance degradation when encoding information. More generally, the ambiguity function of the waveform should be used if the target motion is significant over the pulse duration. Here, it is assumed that this "fast-time" Doppler shift is not significant over a pulse, thus the pulse compressor output can be modeled as a time-shifted and scaled version of the waveform autocorrelation. Define the autocorrelation response of the n_p-th pulse as

$$r(\tau; \boldsymbol{\alpha}_{n_\mathrm{p}}) = \frac{1}{T} \int_0^T s^*(t - \tau; \boldsymbol{\alpha}_{n_\mathrm{p}}) s(t; \boldsymbol{\alpha}_{n_\mathrm{p}}) d\tau, \tag{11}$$

which is necessarily dependent on the CPM symbol sequence $\boldsymbol{\alpha}_{n_\mathrm{p}}$ and is likewise unique on a pulse-by-pulse basis. While the peaks of the autocorrelation responses (i.e., $r(\tau = 0; \boldsymbol{\alpha}_{n_\mathrm{p}})$) across multiple pulses remain coherent (thus permitting slow-time processing of multiple pulses), the sidelobe responses of $r(\tau; \boldsymbol{\alpha}_{n_\mathrm{p}})$ are modulated based on the particular information sequence of each pulse. This *range sidelobe modulation* (RSM) [26], [39], [40] creates a decoherence of the sidelobe responses, and when Doppler processed, spreads energy over the entire Doppler space. For example, Fig. 7 shows the autocorrelation responses[1] $|r(\tau; \boldsymbol{\alpha}_{n_\mathrm{p}})|^2$ (dB)

[1]Only positive delays are plotted since the autocorrelation function is conjugate-symmetric.

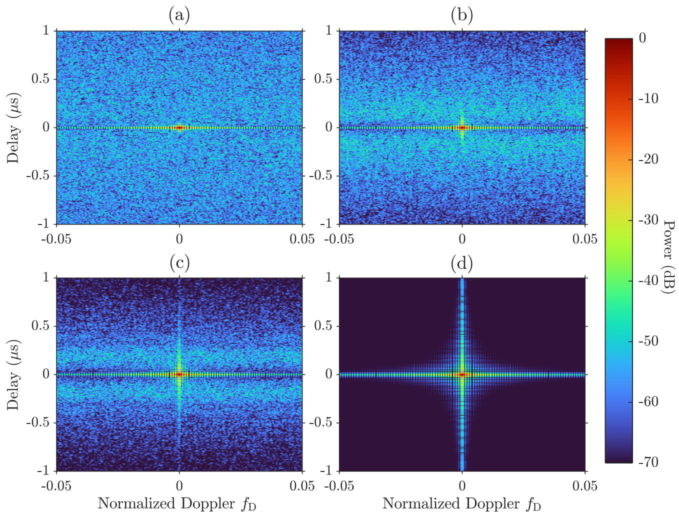

Fig. 8. PARC waveform PSFs $|r_{\mathrm{D}}(\tau, f_{\mathrm{D}})|^2$ (dB) for various modulation indices: (a) $h = \frac{1}{2}$, (b) $h = \frac{1}{4}$, (c) $h = \frac{1}{8}$, and (d) $h = 0$ (i.e., LFM-only). For each case, a total of $N_{\mathrm{p}} = 1000$ independent PARC waveforms were generated with pulsewidth $T = 10$ μs, LFM bandwidth $B = 100$ MHz, binary CPM with $L = 1$ rectangular $q(t)$, and $F_{\mathrm{s}} = 25$ MSymb/s (no guard symbols). Images are zoomed-in to show peak response.

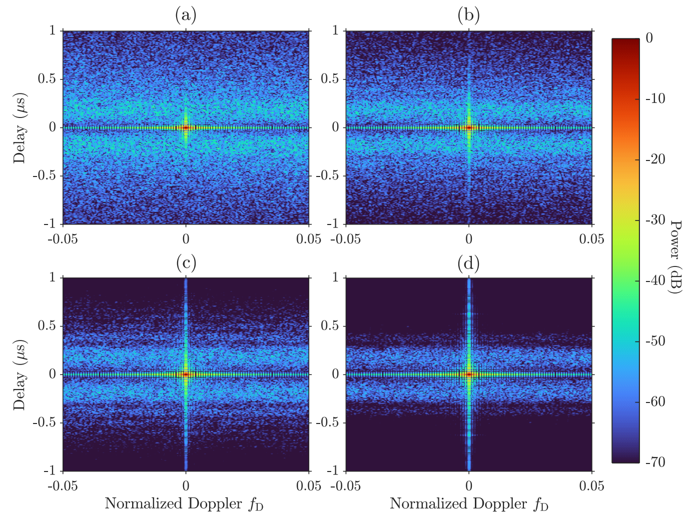

Fig. 9. PARC waveform PSFs $|r_{\mathrm{D}}(\tau, f_{\mathrm{D}})|^2$ (dB) for various symbol rates: (a) $F_{\mathrm{s}} = 50$ MSymb/s, (b) $F_{\mathrm{s}} = 25$ MSymb/s, (c) $F_{\mathrm{s}} = 12.5$ MSymb/s, and (d) $F_{\mathrm{s}} = 6.3$ MSymb/s. For each case, a total of $N_{\mathrm{p}} = 1000$ independent PARC waveforms were generated with pulsewidth $T = 10$ μs, LFM bandwidth $B = 100$ MHz, binary CPM with $L = 1$ rectangular $q(t)$, and $h = \frac{1}{8}$ (no guard symbols). Images are zoomed-in to show peak response.

of three randomly generated PARC waveforms with LFM bandwidth of $B = 100$ MHz and pulsewidth $T = 10$ μs, and binary $(M = 2)$ CPM for $h = \frac{1}{8}$, $F_{\mathrm{s}} = 50$ MSymb/s, $L = 1$ rectangular shaping filter, and no guard symbols $(N_{\mathrm{g}} = 0)$. Note how the mainlobes of the three autocorrelation responses remain similar (zoomed-in view depicted in the inset), but the sidelobe responses are modulated.

The severity of RSM depends on the similarity of the waveform modulation (and thus autocorrelation responses) across pulses. The base radar waveform within the PARC framework provides an inherent similarity across pulses, and the tunability of the CPM parameters naturally provide a means to control the RSM and thus how much sidelobe energy is spread across the range-Doppler space. This trade-off between communications throughput and RSM is inherent to the radar-communication co-designed waveform problem, where the PARC signal structure provides the flexibility to maneuver depending on the prioritization of each function.

To illustrate the spread of energy into the Doppler space caused by RSM, we can observe the delay-Doppler response of a point scatterer at zero-delay and zero-Doppler given a set of N_{p} independently generated PARC pulses in a CPI. Define this impulse response of the range-Doppler radar receiver as the *point spread function* (PSF). Under the assumption of matched filtered delay compression and rectangular Doppler window, the PSF for a set of N_{p} PARC waveforms is expressed as

$$r_{\mathrm{D}}(\tau, f_{\mathrm{D}}; \boldsymbol{\alpha}_0, \ldots, \boldsymbol{\alpha}_{N_{\mathrm{p}}-1}) = \frac{1}{N_{\mathrm{p}}} \sum_{n_{\mathrm{p}}=0}^{N_{\mathrm{p}}-1} r(\tau; \boldsymbol{\alpha}_{n_{\mathrm{p}}}) e^{-j2\pi f_{\mathrm{D}} n_{\mathrm{p}}}, \tag{12}$$

where $-0.5 \leq f_{\mathrm{D}} < 0.5$ is the normalized (or digital) Doppler frequency. For brevity, the PSF is shortened to $r_D(\tau, f_{\mathrm{D}})$, and the dependence of all symbols transmitted during the CPI is implied.

Generated using (12), Fig. 8 illustrates the PSF (in dB) for four sets of PARC waveforms with modulation indices $h = \frac{1}{2}, \frac{1}{4}, \frac{1}{8}$, and 0 (corresponding to Figs. 8(a)–(d), respectively), where the $h = 0$ case represents an LFM-only transmission. For the remaining cases, $N_{\mathrm{p}} = 1000$ independent PARC waveforms were generated with pulsewidth $T = 10$ μs, LFM bandwidth $B = 100$ MHz, binary CPM with $L = 1$ rectangular $q(t)$, and $F_{\mathrm{s}} = 25$ MSymb/s (no guard symbols). Reducing the modulation index clearly reduces the RSM effect observed through the spreading of range sidelobes across Doppler; however, all PARC cases have degraded radar performance compared to the LFM-only case in Fig. 8(d). As h decreases the degree of phase change due to a communication symbol $\alpha_{n_{\mathrm{p}}, n_{\mathrm{s}}}$, which is linear with h (i.e., $h\pi\alpha_{n_{\mathrm{p}}, n_{\mathrm{s}}}$), also decreases. A lower phase deviation in the communication component results in reduced pulse-to-pulse RSM illustrated by the lower spread of power across Doppler.

Figure 9 shows the PSFs (in dB) for symbols rates $F_{\mathrm{s}} = 50, 25, 12.5$, and 6.3 MSymb/s (corresponding to Figs. 9(a)–(d), respectively). The modulation index for all cases is $h = \frac{1}{8}$ and all other PARC waveforms parameters are the same as in Fig. 8. Similar to the reduction of h, it is observed that decreasing F_{s} (increasing T_{s}) reduces the severity of RSM. As the communication symbol interval T_{s} increases, the phase of the communication component changes at a lower rate since each phase change $h\pi\alpha_{n_{\mathrm{p}}, n_{\mathrm{s}}}$ occurs over a time interval of length T_{s}. Since the RSM level in the PSFs is a measure of the similarity between pulse compression responses in a CPI, the reduction of RSM level implies that the similarity between the PARC pulses is improved when the symbol rate F_{s} is decreased.

Note that the ability to control the severity of RSM is not solely a function of modulation index h and symbol rate F_{s}. The RSM response will also be a function of the number of pulses that are integrated N_{p} [40] and other PARC parameters (i.e., modulation order m and shaping filter $q(t)$). For example, increasing the modulation order (with all other parameters fixed) will increase that data throughput without a large change in BER (see Fig. 6), but also increases RSM due to larger phase rotations per symbol. However, the modulation index h and symbol rate F_{s} have the largest effect on the trade-off between radar and communications performance (i.e., RSM, BER, and throughput), which is the reason they are highlighted here.

IV. Clutter Range Sidelobe Modulation and Mitigation via Mismatched Filtering

In a moving target indication (MTI) radar scenario, the primary goal of the system is to detect targets in the presence of undesired scattering called clutter, which must be suppressed via cancellation or windowing across pulses to reduce clutter Doppler sidelobes. Pulse-agile transmission introduce additional complications to the MTI problem via RSM, which arises both in the target and clutter responses. The resulting clutter RSM (C-RSM) establishes a self-interference floor that cannot be canceled with slow-time-only processing, thus hindering target detection performance [40].

To maintain acceptable MTI radar performance, C-RSM must be reduced via signal processing methods. Pulse-agile transmissions introduce a coupling between fast-time and slow-time dimensions that may require joint-domain processing to mitigate C-RSM [51], [52]. Multiple techniques have been developed, but are limited by the high computational complexity of joint-domain processing [53], [54]. Alternatively, fast-time and slow-time dimensions can be approximately decoupled by increasing the similarity between the cross-correlation responses pulse-to-pulse. In the previous section, it was shown that this similarity can be tuned via selection of the PARC communications parameters. In this section, we investigate mitigation of C-RSM via design of the pulse compression filters used on receive (i.e., mismatched filter design [55]–[59]).

A. Clutter Range Sidelobe Modulation

The effect of C-RSM on target estimation performance can be evaluated by building a clutter signal model and determining the resulting clutter power after application of fast-time compression filtering and slow-time Doppler processing. We model the clutter response after pulse compression of the n_{p}-th PRI as the convolution of the fast-time correlation response of the radar receiver with a zero-mean, complex-valued, white Gaussian clutter process $x(\tau)$ as a function of delay τ, and to isolate the pulse-to-pulse variations due to the waveform and pulse compression filter, we assume that the clutter is stationary from pulse-to-pulse and located at zero-Doppler (e.g., ground-based MTI scenario)[2]. Therefore, the clutter response after range compression can be modeled as

$$c(\tau;\boldsymbol{\alpha}_{n_{\mathrm{p}}}) = \int \bar{r}(\eta-\tau;\boldsymbol{\alpha}_{n_{\mathrm{p}}})x(\eta)d\eta \tag{13}$$

where

$$\bar{r}(\tau;\boldsymbol{\alpha}_{n_{\mathrm{p}}}) = \int_0^T w(\tau-t;\boldsymbol{\alpha}_{n_{\mathrm{p}}})s(t;\boldsymbol{\alpha}_{n_{\mathrm{p}}})dt \tag{14}$$

is the n_{p}-th cross-correlation function for any pulse compression filter $w(t;\boldsymbol{\alpha}_{n_{\mathrm{p}}})$ (i.e., matched or mismatched) designed according to the symbol sequence $\boldsymbol{\alpha}_{n_{\mathrm{p}}}$.

Discretizing the waveform $s(t;\boldsymbol{\alpha}_{n_{\mathrm{p}}})$ and filter $w(t;\boldsymbol{\alpha}_{n_{\mathrm{p}}})$ at sampling rate $F_{\mathrm{samp}} = \frac{1}{T_{\mathrm{samp}}}$, we can obtain the discrete-time correlation vector for the n_{p}-th pulse as

$$\bar{\mathbf{r}}_{n_{\mathrm{p}}} = \mathbf{S}_{n_{\mathrm{p}}}\mathbf{w}_{n_{\mathrm{p}}}, \tag{15}$$

where

$$\mathbf{w}_{n_{\mathrm{p}}} = [w_{0,n_{\mathrm{p}}}, w_{1,n_{\mathrm{p}}}, \dots, w_{N_{\mathrm{w}}-1,n_{\mathrm{p}}}]^T \tag{16}$$

is the length-N_{w} discretized filter in which $w_{n,n_{\mathrm{p}}} = w(nT_{\mathrm{samp}};\boldsymbol{\alpha}_{n_{\mathrm{p}}})$, and

$$\mathbf{S}_{n_{\mathrm{p}}} = \begin{bmatrix} s_{0,n_{\mathrm{p}}} & 0 & \cdots & 0 \\ \vdots & s_{0,n_{\mathrm{p}}} & & \vdots \\ s_{N-1,n_{\mathrm{p}}} & \vdots & \ddots & 0 \\ 0 & s_{N-1,n_{\mathrm{p}}} & & s_{0,n_{\mathrm{p}}} \\ \vdots & & \ddots & \vdots \\ 0 & & \cdots & s_{N-1,n_{\mathrm{p}}} \end{bmatrix} \tag{17}$$

is the $(N+N_{\mathrm{w}}-1)\times N_{\mathrm{w}}$ waveform convolution matrix for discretized waveform samples $s_{n,n_{\mathrm{p}}} = s(nT_{\mathrm{samp}};\boldsymbol{\alpha}_{n_{\mathrm{p}}})$ that comprise the length $N = TF_{\mathrm{samp}}$ waveform vector

$$\mathbf{s}_{n_{\mathrm{p}}} = [s_{0,n_{\mathrm{p}}}, s_{1,n_{\mathrm{p}}}, \dots, s_{N-1,n_{\mathrm{p}}}]^T. \tag{18}$$

Therefore, vector $\bar{\mathbf{r}}_{n_{\mathrm{p}}}$ is $(N+N_{\mathrm{w}}-1)\times 1$. Using this discrete formulation, the clutter response after pulse compression of the n_{p}-th pulse can be expressed as the vector inner-product

$$c_{n_{\mathrm{p}}} = \bar{\mathbf{r}}_{n_{\mathrm{p}}}^T\mathbf{x}, \tag{19}$$

where $\mathbf{x}$ is a $(N+N_{\mathrm{w}}-1)\times 1$ zero-mean, white complex Gaussian random vector with sample variance σ_{x}^2. Note that the dependence on information sequence $\boldsymbol{\alpha}_{n_{\mathrm{p}}}$ is implied via the pulse index n_{p}.

Aggregating the clutter samples over the entire CPI (N_{p} pulses) yields

$$\mathbf{c} = [c_0, c_1, \dots, c_{N_{\mathrm{p}}-1}]^T = \bar{\mathbf{R}}^T\mathbf{x}, \tag{20}$$

for

$$\bar{\mathbf{R}} = [\bar{\mathbf{r}}_0, \bar{\mathbf{r}}_1, \dots, \bar{\mathbf{r}}_{N_{\mathrm{p}}-1}], \tag{21}$$

where the dependency on the set of information sequences $\boldsymbol{\alpha}_0, \dots, \boldsymbol{\alpha}_{N_{\mathrm{p}}-1}$ for $\mathbf{c}$ and $\bar{\mathbf{R}}$ has been suppressed for brevity. The expected Doppler PSD due to clutter can be found via the discrete-time Fourier transform (DTFT) of $\mathbf{c}$ modified by a length-N_{p} taper vector $\mathbf{t}$, i.e., $\mathcal{E}_{\mathbf{c}}\{|(\mathbf{t}\odot\mathbf{a}(f_{\mathrm{D}}))^H\mathbf{c}|^2\}$, where $\mathcal{E}_{\mathbf{c}}\{\bullet\}$ is the statistical expectation over $\mathbf{c}$, $\odot$ is the element-wise Hadamard product, and

$$\mathbf{a}(f_{\mathrm{D}}) = [1, e^{j2\pi f_{\mathrm{D}}}, \dots, e^{j2\pi f_{\mathrm{D}}(N_{\mathrm{p}}-1)}]^T \tag{22}$$

[2]Note that the statistics of the clutter process $x(\tau)$ would also be a function of range due to spherical spreading losses; however, we assume that the statistics are homogenous for the purposes of this analysis.

is the length-N_p DTFT vector for normalized Doppler frequency f_D. Since the covariance of $\mathbf{x}$ is an identity matrix scaled by σ_x^2, this expectation can be found in closed-form. To remove the dependence on the clutter variance σ_x^2, we peak-normalize the Doppler response knowing that the clutter is located at zero-Doppler. The peak-normalized Doppler PSD due to zero-Doppler clutter for a given set of N_p PARC pulses can be shown to be

$$P_\mathrm{C}(f_\mathrm{D}) = \frac{(\mathbf{t}\odot\mathbf{a}(f_\mathrm{D}))^H\bar{\mathbf{R}}^T\bar{\mathbf{R}}^*(\mathbf{t}\odot\mathbf{a}(f_\mathrm{D}))}{\mathbf{t}^H\bar{\mathbf{R}}^T\bar{\mathbf{R}}^*\mathbf{t}}. \tag{23}$$

Note that this Doppler PSD is based on the specified communications sequences defined in $\boldsymbol{\alpha}_{n_\mathrm{p}}$ for $n_\mathrm{p}=0,1,\ldots,N_\mathrm{p}-1$. A derivation of the expression in (23) is provided in the Appendix.

Similar to (4), the average Doppler-spread power caused by C-RSM (denoted as C-RSM power) is determined by considering (for fixed CPM-PARC parameters) the entire set of possible CPM-PARC waveforms $s(t;\tilde{\boldsymbol{\alpha}}_k)$ for $k=0,\cdots,2^{N_b}-1$. Denote the corresponding set of length-N waveform vectors as $\tilde{\mathbf{s}}_k$, length-N_w filters as $\tilde{\mathbf{w}}_k$, and convolution matrices as $\tilde{\mathbf{S}}_k$. Define $\bar{\mathbf{r}}_\mu = \mathcal{E}_{\tilde{\boldsymbol{\alpha}}_k}\{\tilde{\mathbf{S}}_k\tilde{\mathbf{w}}_k\}$ as the mean cross-correlation response, where the expectation is over the entire set of possible symbol sequences $\tilde{\boldsymbol{\alpha}}_k$. We can then define a *mismatch metric* [43] as the expected pulse-to-pulse variance of the correlation response,

$$\Delta_\mathrm{MM} = \mathcal{E}_{\tilde{\boldsymbol{\alpha}}_k}\{\|\tilde{\mathbf{S}}_k\tilde{\mathbf{w}}_k - \bar{\mathbf{r}}_\mu\|_2^2\}. \tag{24}$$

The mismatch metric not only quantifies the average incoherence across the filter responses, but can also be used to find the expected C-RSM power in the range-Doppler response after Doppler processing with an arbitrary number of pulses in a CPI and an arbitrary taper $\mathbf{t}$. For a particular set of CPM-PARC parameters (fixed $h, M, N_\mathrm{s}, q(t)$), the peak-normalized C-RSM power is [40]

$$P_\text{C-RSM}(N_\mathrm{p},\mathbf{t},\Delta_\mathrm{MM},\bar{\mathbf{r}}_\mu) = \frac{\Delta_\mathrm{MM}}{N_\mathrm{p}\,L_\mathrm{st}(\mathbf{t})\,\|\bar{\mathbf{r}}_\mu\|_2^2}, \tag{25}$$

where $0\le L_\mathrm{st}(\mathbf{t})\le 1$ is the SNR loss of the slow-time Doppler taper defined as [60]

$$L_\mathrm{st}(\mathbf{t}) = \frac{|\sum_{n_\mathrm{p}=0}^{N_\mathrm{p}-1} t_{n_\mathrm{p}}|^2}{N_\mathrm{p}\|\mathbf{t}\|_2^2}. \tag{26}$$

Note that the normalized C-RSM power does not vary with f_D and is thus evenly spread over the Doppler space.

The expression in (23) provides the expected peak-normalized Doppler PSD due to clutter for a particular set of N_p waveforms, and (25) gives the expected peak-normalized C-RSM power level (i.e., the Doppler-spread power caused by C-RSM) over the entire set of possible symbol sequences for any set of N_p waveforms. Both (23) and (25) implicitly incorporate both the pulse compression filter and Doppler taper $\mathbf{t}$ into their calculations. Furthermore, these expressions assume that the clutter statistics are homogeneous in range and localized at zero-Doppler. Note that internal clutter motion and/or moving platforms will spread clutter power over Doppler; therefore, the peak normalizations in (23) and (25) will not hold for these cases. However, it is expected that these

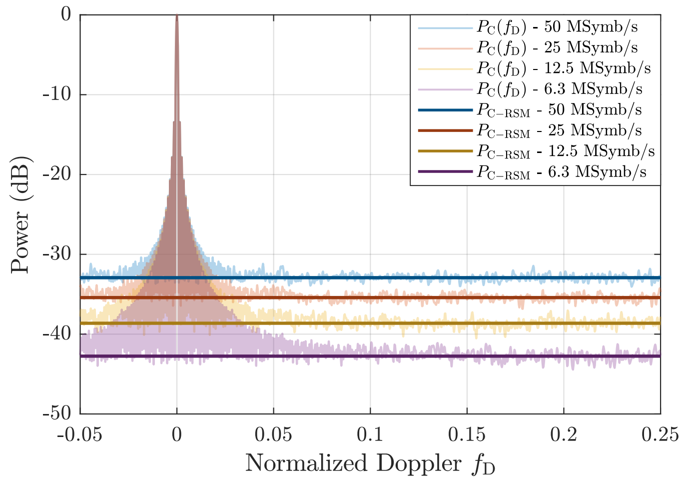

Fig. 10. The expected C-RSM power $P_\text{C-RSM}$ (dB) and expected Doppler PSD due to clutter $P_\mathrm{C}(f_\mathrm{D})$ (dB) assuming rectangular Doppler taper $\mathbf{t}$ and matched filter delay compression for a set of $N_\mathrm{p}=1000$ PARC waveforms for pulsewidth of $T=10$ μs, LFM bandwidth $B=100$ MHz, binary CPM with $L=1$ rectangular $q(t)$, $h=1/8$, no guard symbols, and four different symbols rates: $F_\mathrm{s}=50$ MSymb/s (blue), $F_\mathrm{s}=25$ MSymb/s (red), $F_\mathrm{s}=12.5$ MSymb/s (yellow), and $F_\mathrm{s}=6.3$ MSymb/s (purple).

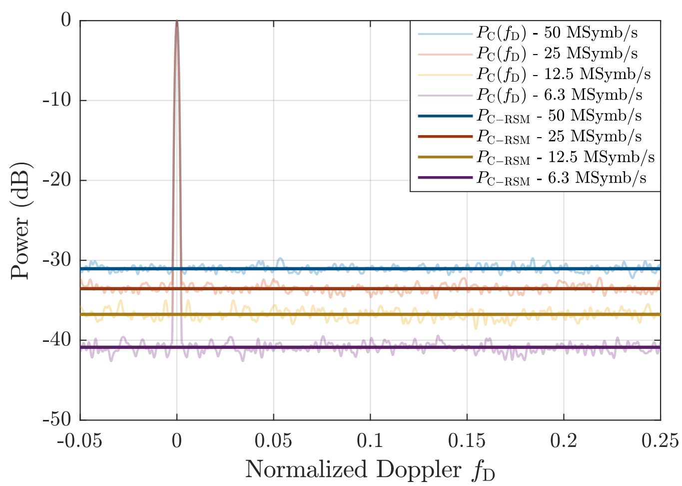

Fig. 11. The expected C-RSM power $P_\text{C-RSM}$ (dB) and expected Doppler PSD due to clutter $P_\mathrm{C}(f_\mathrm{D})$ (dB) assuming -60 dB Taylor taper $\mathbf{t}$ and matched filter delay compression for a set of $N_\mathrm{p}=1000$ PARC waveforms for pulsewidth of $T=10$ μs, LFM bandwidth $B=100$ MHz, binary CPM with $L=1$ rectangular $q(t)$, $h=1/8$, no guard symbols, and four different symbols rates: $F_\mathrm{s}=50$ MSymb/s (blue), $F_\mathrm{s}=25$ MSymb/s (red), $F_\mathrm{s}=12.5$ MSymb/s (yellow), and $F_\mathrm{s}=6.3$ MSymb/s (purple).

expressions can be generalized for clutter processes that are spread in Doppler (i.e., not localized at zero Doppler).

As an example, consider processing $N_\mathrm{p}=1000$ PARC pulses using matched filter processing $(w(t;\boldsymbol{\alpha}_{n_\mathrm{p}})=s^*(-t;\boldsymbol{\alpha}_{n_\mathrm{p}}))$ and a rectangular Doppler taper $t_{n_\mathrm{p}}=1$. Figure 10 shows the expected (normalized) Doppler PSD due to clutter for a generated set of PARC waveforms using (23) and the expected (normalized) C-RSM power over the entire set of possible PARC waveforms using (25) for four different symbol rates: $F_\mathrm{s}=50, 25, 12.5,$ and 6.3 MSymb/s. For this case, we use a pulsewidth of $T=10$ μs, LFM bandwidth of $B=100$ MHz, binary CPM with $L=1$ rectangular $q(t)$, $h=\frac{1}{8}$, and no guard symbols. For clutter

PSD $P_{\mathrm{C}}(f_{\mathrm{D}})$, the sinc spectral sidelobes of the rectangular Doppler window dominate at lower Doppler frequencies; however, a floor is formed once the C-RSM power begins to dominate, which is predicted via $P_{\mathrm{C-RMS}}$ in (25). This floor cannot be removed via slow-time-only processing because the Doppler spectrum is white; therefore, target detection/estimation performance is limited due to C-RSM. The expected normalized C-RSM powers for Fig. 10 are -31.9 dB, -35.4 dB, -38.6 dB, and -42.8 dB for symbol rates $F_{\mathrm{s}} = 50$, 25, 12.5, and 6.3 MSymb/s, respectively. Figure 11 shows the same cases as in Fig. 10 but with a -60 Taylor taper applied in slow-time. The spectral sidelobes of the Doppler responses are mitigated; however, the C-RSM power remains, demonstrating that slow-time tapering cannot mitigate the C-RSM floor. Furthermore, the slow-time filter loss $L_{\mathrm{st}}(\mathbf{t})$ has increased the normalized C-RSM powers by the Taylor taper SNR loss of 1.9 dB.

As discussed in Section III-B, Figs. 10 and 11 both demonstrate that C-RSM power can be reduced via selection of the communications parameters (e.g., the symbol rate F_{s}). However, trading communications performance for improvements in radar performance is not always desirable in a co-designed joint system. Alternatively, we can improve the pulse compression filtering $w(t; \boldsymbol{\alpha}_{n_{\mathrm{p}}})$ (via mismatched filtering) to largely mitigate C-RSM power caused by pulse agility without sacrificing communications performance.

B. Mitigating C-RSM via Mismatched Filtering

To maintain acceptable radar performance, C-RSM should be reduced, which can be achieved by a combination of waveform design [33], [41] and radar receive processing [26], [27], [43], [44], [51]–[54], [61]. The detrimental effect of C-RSM shown in the previous section is caused by the pulse-agile transmission structure of PARC, which couples the fast-time and slow-time dimensions [51]. Previous joint-domain processing approaches were developed for arbitrary pulse-agile emissions in [51], [52] to maximize the signal-to-noise-plus-interference ratio (SINR) on receive. Furthermore, in [53], [54], reduced-complexity implementations of the maximum SINR approach in [51], [52] were developed, though the computational complexity is still significant. These approaches are all based on solutions to large inverse problems with dimensionality on the order of NN_{p}.

Alternatively, receive processing can be simplified by optimizing each pulse compression filter individually to produce a common desired correlation response (see [26], [27]), thus mitigating RSM and decoupling the fast-time and slow-time dimensions. One of the attractive features of the CPM-PARC approach is the high data throughput. As a result, the number of distinct PARC waveforms 2^{N_b} is quite large, which prohibits joint optimization of the filter responses based on the set of waveforms as in [26], [27] that is only feasible for a small number of waveforms[3]. Here, we address receive filter design for the purpose of reducing the C-RSM within the CPM-PARC framework [43] by establishing a *fixed* (i.e., not jointly optimized [26], [27]) desired common filter response. Given this common response, the receive filter for each transmitted PARC waveform is independently computed.

Ideally, the objective for receive filter design is to find the associated discrete-time filter $\tilde{\mathbf{w}}_k$ satisfying the matrix representation of convolution denoted as [26]

$$\tilde{\mathbf{S}}_k \tilde{\mathbf{w}}_k = \mathbf{d}, \tag{27}$$

where $\mathbf{d}$ is a $(N + N_{\mathrm{w}} - 1) \times 1$ desired correlation response common across all pulses. It was discussed in [26] that (27) cannot be achieved with finite-length filters for more than two distinct waveforms. Therefore, to reduce RSM for an arbitrary number of waveforms, the objective in receive filter design is to minimize the average incoherence among the filter responses. An important consideration in the mismatched filter design problem is the incurred mismatch loss (also known as white noise gain) due to deviation from the matched filter. We can calculate this fast-time filter loss via [56]–[58]

$$L_{\mathrm{ft}}(\tilde{\mathbf{w}}_k) = \frac{|\tilde{\mathbf{w}}_k^T \mathbf{v}_k|^2}{\|\tilde{\mathbf{w}}_k\|_2^2 \|\mathbf{v}_k\|_2^2} \tag{28}$$

for $0 \leq L_{\mathrm{ft}}(\tilde{\mathbf{w}}_k) \leq 1$, where

$$\mathbf{v}_k = [0, \ldots, 0, \tilde{s}_{N-1,k} \ldots, \tilde{s}_{0,k}, 0, \ldots, 0]^T \tag{29}$$

is the waveform model at the matched delay of the filter (center row of $\tilde{\mathbf{S}}_k$). Note the waveform samples in (29) are reversed due to the convolutional model.

The mismatched filter design problem can then be viewed as a minimization of the distance between the true and desired cross-correlation responses while constraining the mismatch loss above some value ρ. The resulting optimization problem can be expressed as [56]

$$\begin{aligned} \min_{\tilde{\mathbf{w}}_k^*} \quad & \|\tilde{\mathbf{S}}_k \tilde{\mathbf{w}}_k - \mathbf{d}\|_2^2 \\ \text{s.t.} \quad & L_{\mathrm{ft}}(\tilde{\mathbf{w}}_k) \geq \rho \end{aligned}, \tag{30}$$

which is a non-convex problem in $\tilde{\mathbf{w}}_k$ due to the inequality constraint being non-convex [56]. However, for a quadratic objective with a single quadratic inequality constraint, strong duality holds for any definiteness of matrix provided the Hessian of the Lagrangian is positive semi-definite and Slater's condition is satisfied [62, p. 653] (i.e., there exists a $\tilde{\mathbf{w}}_k$ such that $L_{\mathrm{ft}}(\tilde{\mathbf{w}})$ is strictly feasible); therefore, (30) can be globally solved via the Lagrange dual problem [56]. While the mismatched filter problem is likewise an inverse problem, the techniques discussed in [51]–[54], [61] have much larger dimensionality, where the mismatched filtering problem comparatively has much lower computational complexity and can

[3]The approaches in [26], [27] can be implemented on a CPI-to-CPI basis. Such an implementation would apply each approach to the set of distinct PARC waveforms transmitted within a CPI, which has at most N_{p} waveforms. When the set of waveforms changes in the next CPI, each approach is applied to the new set and so on. As a result, these approaches can be applied to the CPM-PARC despite $2^{N_{\mathrm{b}}}$ being in general very large. However, for practical values of N_{p}, the resulting computational complexity is still very high.

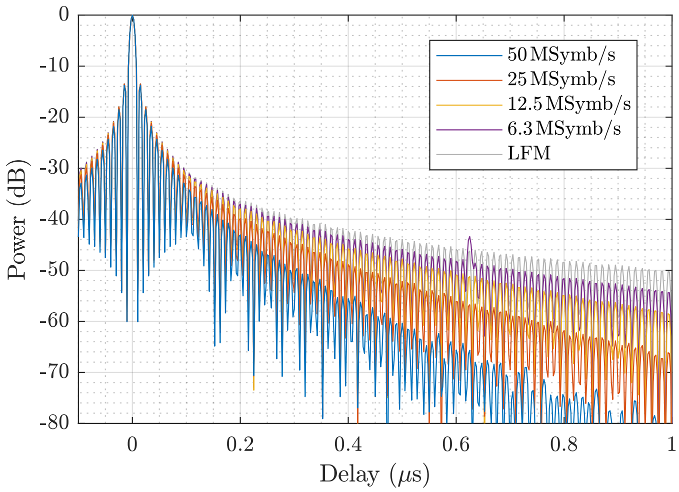

Fig. 12. The desired correlation responses (mean correlation responses using matched filtering) $\mathbf{d} = \mathcal{E}_{\tilde{\boldsymbol{\alpha}}_k}\{\tilde{\mathbf{S}}_k \mathbf{v}_k^*\}$ for PARC waveforms for pulsewidth of $T = 10$ μs, LFM bandwidth $B = 100$ MHz, binary CPM with $L = 1$ rectangular $q(t)$, $h = 1/8$, no guard symbols, and four different symbols rates: $F_\text{s} = 50$ MSymb/s (blue), $F_\text{s} = 25$ MSymb/s (red), $F_\text{s} = 12.5$ MSymb/s (yellow), $F_\text{s} = 6.3$ MSymb/s (purple), and LFM-only (gray).

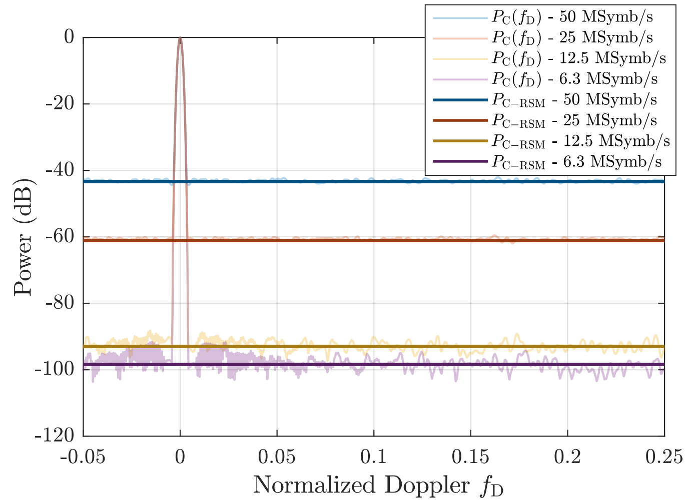

Fig. 13. The expected C-RSM power $P_\text{C-RSM}$ (dB) and expected Doppler PSD due to clutter $P_\text{C}(f_\text{D})$ (dB) assuming -120 dB Taylor taper $\mathbf{t}$ and mismatched filter delay compression for a set of $N_\text{p} = 1000$ PARC waveforms for pulsewidth of $T = 10$ μs, LFM bandwidth $B = 100$ MHz, binary CPM with $L = 1$ rectangular $q(t)$, $h = 1/8$, no guard symbols, and four different symbols rates: $F_\text{s} = 50$ MSymb/s (blue), $F_\text{s} = 25$ MSymb/s (red), $F_\text{s} = 12.5$ MSymb/s (yellow), and $F_\text{s} = 6.3$ MSymb/s (purple).

be solved efficiently due to its Toeplitz structure [54]. The resulting mismatched filter takes the form

$$\tilde{\mathbf{w}}_k = \left(\tilde{\mathbf{S}}_k^H \tilde{\mathbf{S}}_k + \lambda(\rho\|\mathbf{v}_k\|_2^2 \mathbf{I}_{N_\text{w}} - \mathbf{v}_k^* \mathbf{v}_k^T)\right)^{-1} \tilde{\mathbf{S}}_k^H \mathbf{d}, \tag{31}$$

where $\mathbf{I}_{N_\text{w}}$ is the $N_\text{w} \times N_\text{w}$ identity matrix and λ is the Lagrange multiplier designed to meet the mismatch loss constraint in (30).

Note that the objective function in (30) takes a similar form to the mismatch metric in (24). Therefore, to reduce the pulse-to-pulse variance, it is natural to set the common desired response to the mean autocorrelation response, $\mathbf{d} = \mathcal{E}_{\tilde{\boldsymbol{\alpha}}_k}\{\tilde{\mathbf{S}}_k \mathbf{v}_k^*\}$, which is dependent on the particular selection of PARC parameters. Also note that the mismatched filtering problem when $\mathbf{d} = \mathcal{E}_{\tilde{\boldsymbol{\alpha}}_k}\{\tilde{\mathbf{S}}_k \mathbf{v}_k^*\}$ only reduces the pulse-to-pulse correlation variance and does not minimize correlation sidelobes of $\mathcal{E}_{\tilde{\boldsymbol{\alpha}}_k}\{\tilde{\mathbf{S}}_k \mathbf{v}_k^*\}$. Here, we focus on solely reducing C-RSM, where joint minimization of the pulse-to-pulse variance and mean correlation sidelobes will be considered in future work.

As an example of the effectiveness of mismatch filtering to reduce C-RSM power, consider the transmission cases from Figs. 10 and 11. Mismatched filters are designed for these PARC transmissions using (31) for filter length $N_\text{w} = 3N$ with $\mathbf{d}$ set to the expected autocorrelation response (i.e., $\mathbf{d} = \mathcal{E}_{\tilde{\boldsymbol{\alpha}}_k}\{\tilde{\mathbf{S}}_k \mathbf{v}_k^*\}$), and are generated using the techniques in [56] for a loss constraint of 2 dB ($\rho = 10^{-2/10} = 0.631$). Figure 12 shows the desired correlation responses $\mathbf{d}$ used in the mismatched filter design problem compared to the LFM-only autocorrelation (gray). Note that the correlation responses are similar to that of the base radar waveform (i.e., LFM); however, the sidelobes begin to decorrelate as the symbol rate increases. Figure 13 shows the resulting expected C-RSM power $P_\text{C-RSM}$ from (25), and the expected clutter PSD $P_\text{C}(f_\text{D})$ from (23) given the set of waveforms and corresponding mismatched filters. Here, a -120 dB Taylor window (2.9 dB of loss) is used to ensure agreement between the floor of $P_\text{C}(f_\text{D})$ and the relative C-RSM power $P_\text{C-RSM}$. The lower data rate cases (i.e., 12.5 and 6.25 MSymb/s), have significantly lowered C-RSM power after applying mismatched filtering.

The expected normalized C-RSM powers for a rectangular Doppler taper (i.e., the C-RSM power in Fig. 13 minus 2.9 dB) are -46.3 dB, -64.1 dB, -96.0 dB, and -101.4 dB for symbol rates $F_\text{s} = 50$, 25, 12.5, and 6.3 MSymb/s, respectively. When compared to the matched filtering cases shown in Fig. 10, the application of mismatched filtering leads to C-RSM improvements of 13.4 dB (50 MSymb/s), 28.7 dB (25 MSymb/s), 57.3 dB (12.5 MSymb/s), and 58.6 dB (6.3 MSymb/s), showing that the improvement due to mismatched filtering is nonlinear versus symbol rate. By designing the pulse compression filters of each PARC pulse to fit the mean correlation response, we have reduced the pulse-to-pulse variance and C-RSM power and effectively decoupled the fast-time and slow-time dimensions for a modest reduction in SNR loss. The degree to which C-RSM is reduced is highly dependent on the selection of PARC parameters (e.g., data rate), and must be considered in the radar and communications performance trade-space.

V. Open-Air Experimental Demonstration

The co-designed DFRC performance of the PARC waveform was tested in an open-air environment at the University of Kansas. Three different transmission cases were tested and processed: two PARC cases and an LFM control case. The radar and communication parameters for these cases can be found in Table I. The PARC waveforms selected for test have two symbol rates (25, 50 MSymb/s) and two modulation indices ($h = \frac{1}{2}$ and $h = \frac{1}{8}$), with $L = 3$ raised-cosine (RC) shaping filter $q(t)$. Deviating slightly from the prior analysis, the PARC transmissions were interleaved with LFM, where

TABLE I
TRANSMISSION CASE PARAMETERS

	Case 1	Case 2	Case 3
Bandwidth B (MHz)	100	100	100
Pulsewidth T (μs)	10	10	10
Center freq. (GHz)	3.4	3.4	3.4
Pulse repetition interval (μs)	40	40	40
Coherent processing interval (ms)	40	40	40
Pulses in CPI N_{p}	1000	1000	1000
Modulation index h	$1/2$	$1/8$	–
Modulation order m (bits/symb)	1	1	–
Shaping filter $q(t)$	RC	RC	–
Filter duration L (symbols)	3	3	–
Symbol rate F_{s} (MSymb/s)	25	50	–
Symbols per pulse N_{s}	250	500	–
Effective symbol rate (MSymb/s)	2.8884	5.7519	–
Guard time T_{g} (μs)	0.36	0.38	–
Guard symbols N_{g}	9	19	–

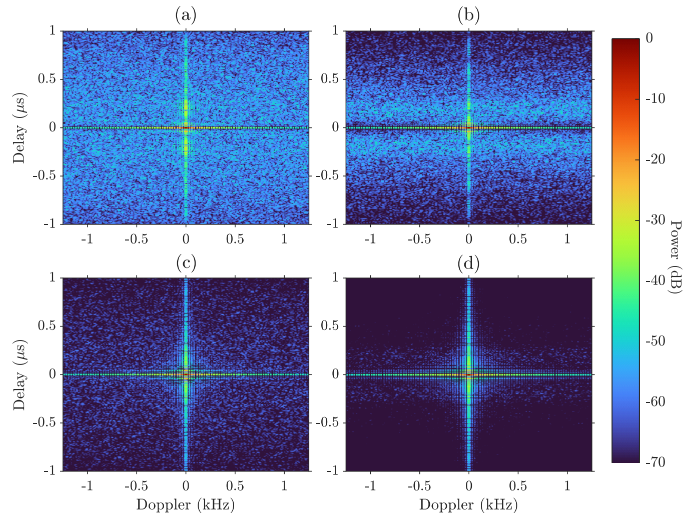

Fig. 14. Loopback PARC waveform PSFs for: (a) Case 1 - Matched Filter, (b) Case 2 - Matched Filter, (c) Case 1 - Mismatched Filter, and (d) Case 2 - Mismatched Filter. For each case, a total of $N_{\mathrm{p}} = 1000$ alternating PARC and LFM waveforms were generated with pulsewidth $T = 10$ μs, LFM bandwidth $B = 100$ MHz, and binary CPM with $L = 3$ raised-cosine $q(t)$. Images are zoomed-in to show peak response.

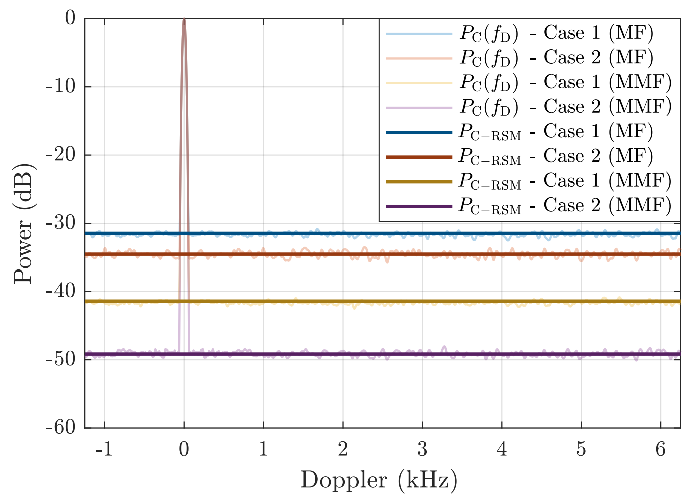

Fig. 15. The expected C-RSM power $P_{\text{C-RSM}}$ and expected Doppler PSD due to clutter $P_{\mathrm{C}}(f_{\mathrm{D}})$ assuming -60 dB Taylor taper $\mathbf{t}$ for a set of $N_{\mathrm{p}} = 1000$ alternating LFM and PARC waveforms with pulsewidth of $T = 10$ μs, LFM bandwidth $B = 100$ MHz, and binary CPM with $L = 3$ raised-cosine $q(t)$ for: Case 1 matched filtering (blue), Case 2 matched filtering (red), Case 1 mismatched filtering (yellow), and Case 2 mismatched filtering (purple).

the LFM pulses were used to facilitate synchronization at the communication receiver. Taking into account the guard symbols, pulse duty cycle, and alternating LFM and PARC, the effective symbol rate (and bit rate) is 2.88845 and 5.7519 MSymb/s for Cases 1 and 2, respectively.

A. Radar Loopback Capture Performance

To generate the matched and mismatched filters while incorporating possible distortions that inevitably arise from the transmit and/or receive chains, the three CPI cases were captured in a loopback configuration where the transmit chain is directly connected to the radar receive chain through an attenuator. The transmit chain consists of a Tektronix 70002A Arbitrary Waveform Generator (AWG), bandpass filter, and amplifier. The receive chain consists of a bandpass filter, low-noise amplifier, and Rohde and Schwarz FSW26 real-time spectrum analyzer (RSA) to capture the in-phase and quadrature signal components. The three CPI cases were generated directly at passband using the AWG and captured on the RSA at a sampling rate of $F_{\mathrm{samp}} = 200$ MHz for analysis and filter generation.

The loopback-captured waveforms were used to create the matched and mismatched filters for radar processing. The matched filters for each case are simply the direct captures (time-reversed and complex-conjugated), which includes any amplifier distortion. For each PARC case, the autocorrelation responses for all captured pulses in the sequence are coherently averaged to obtain the mean correlation response, which in turn is used as the desired response $\mathbf{d}$ for the design of the PARC mismatched filters via (31). Similar to Section IV-B, the mismatched filters are designed for a length of $N_{\mathrm{w}} = 3N$ and for a loss constraint of 2 dB ($\rho = 10^{-2/10} = 0.631$).

Using the loopback-captured waveforms and pulse compression filters, the expected radar performance for both the matched and mismatched filter banks can be evaluated via the PSF (12), the Doppler PSD (23), and C-RSM power (25). The PSF for the mismatched filters can be generated by substituting (11) for (14) in (12). Figure 14 shows the PSFs for each PARC case for both matched and mismatched filter processing and zoom-in to show the peak response. The mismatched filters are effective in reducing the RSM levels relative to their matched filter counterparts, with the median bin value of the observed data in Fig. 14 reducing by approximately 11 dB and 15 dB for Cases 1 and 2, respectively. These levels of improvement can likewise be seen in Fig. 15 (assuming a -60 dB Taylor taper) with the expected C-RSM power and expected Doppler PSD reduced by approximately the same amounts.

B. Open-Air Experiment

For the open-air testing, the transmit and receive chains were connected to two S-band dishes placed in a quasi-monostatic configuration and operated in a simultaneous transmit and receive mode. The direct path leakage between the

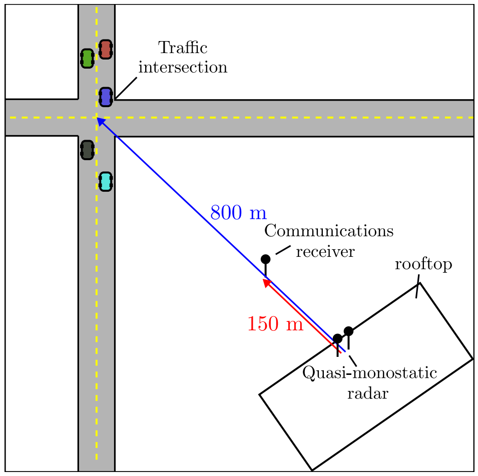

Fig. 16. Configuration of open-air experiment with quasi-monostatic radar placed on a rooftop, communications receiver at a distance of approximately 150 m, and a traffic intersection at a distance of approximately 800 m (not to scale).

transmit and receive antennas and the near-in scattering acts as strong clutter components between 0 and 100 meters. The radar antennas were placed on a rooftop and oriented towards a traffic intersection in Lawrence, Kansas approximately 800 meters away from the radar testbed and contained multiple targets-of-opportunity (cars and trucks). The communications receive antenna was located in a parking lot approximately 150 meters away from the radar and placed to obtain a strong line-of-sight path between the radar testbed and traffic intersection. Figure 16 shows an illustration of the experiment configuration. The communications receiver consisted of an S-band antenna, low-noise amplifier, and Rohde and Schwarz FSW26 RSA to capture the in-phase and quadrature signals. Each case was transmitted sequentially (one after the other) to illuminate a similar scene for comparison. The three transmission cases were looped for approximately two seconds for data capture at both the radar and communications receivers at a rate of $F_{\rm samp} = 200$ MHz.

1) Communication Results: The placement of the communications antenna to obtain strong line-of-sight path was to mitigate the need of equalization methods due to delay dispersion of the channel (i.e., multipath). The single strong path allows for simple time and phase alignment of the pulses for demodulation. Furthermore, the independent reference oscillator of the communications receiver required estimation of the frequency offset between the systems. The LFM-only pulses interspersed throughout the PARC transmissions are used as pilots for the estimation of these quantities. The exact method of synchronization involved matched filtering to each LFM pulse, estimating the delay, phase, and reference frequency offset via fast-time and slow-time processing. There are many methods to estimate time, phase, and frequency offsets of systems [42], and once estimated the received envelopes can be synchronized and the LFM phase function $\psi(t)$ can be removed via (9).

A total of eight CPIs were captured for each case resulting in a total of 924,288 bits transmitted for Case 1 and 1,840,608

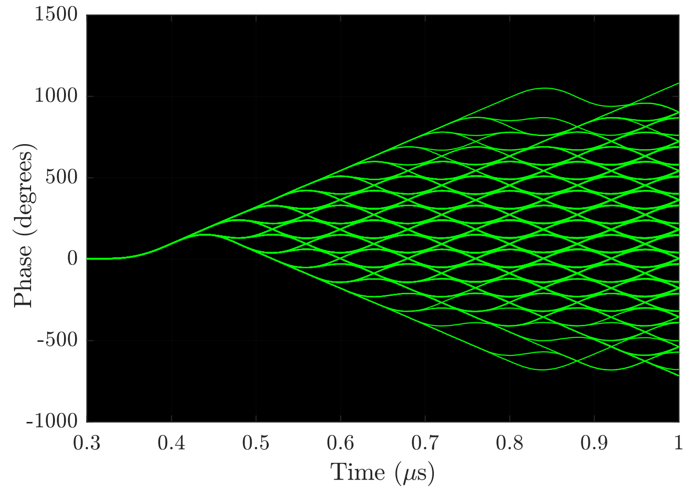

Fig. 17. Unwrapped phase trajectories of all Case 1 PARC pulses after time, phase, and frequency synchronization, and removal of the LFM phase function.

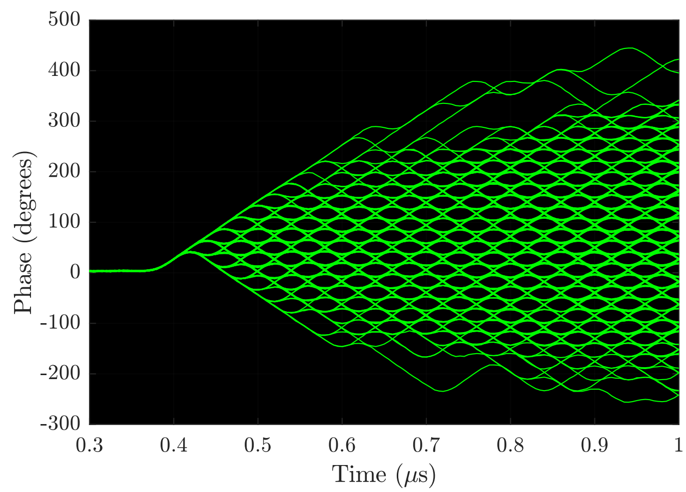

Fig. 18. Unwrapped phase trajectories of all Case 2 PARC pulses after time, phase, and frequency synchronization, and removal of the LFM phase function.

bits transmitted for Case 2. The strong direct path component yields an estimated $E_{\rm s}/N_0 = 50$ dB for Case 1 and $E_{\rm s}/N_0 = 47$ dB for Case 2. The 3 dB of difference in SNR between the cases is to be expected because the symbol period of Case 2 is half that of Case 1. All bits in the eight captured CPIs for both cases were correctly demodulated via the Viterbi algorithm (i.e., zero bit errors) demonstrating the capability to embed information onto a radar transmission via the PARC framework.

The ability to distinguish the symbol sequences can be seen via the unwrapped phase functions of the synchronized open-air PARC pulses after removal of the LFM phase function for Case 1 shown Fig. 17 and Case 2 shown in Fig. 18. The unwrapped phase functions show the guard symbols near the beginning of the pulse and the unwrapped phase trajectory pattern of the CPM phase function once the symbols become non-zero. The regularity of the patterns demonstrate a good synchronization accuracy and high SNR of the received pulses. Note that the first two symbols of each pulse (after the guard time) were set to 1 (i.e., $\alpha_{n_{\rm p},N_{\rm g}+1} = \alpha_{n_{\rm p},N_{\rm g}+2} = 1$) to ensure

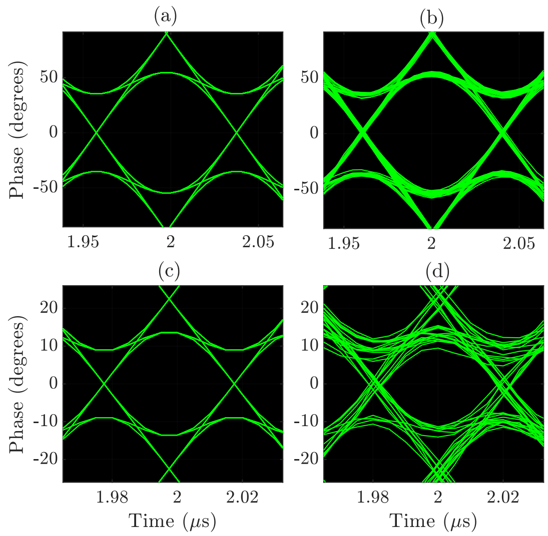

Fig. 19. Zoomed-in phase responses of all PARC pulses after synchronization and removal of the LFM phase function for: (a) ideal Case 1, (b) open-air Case 1, (c) ideal Case 2, and (d) open-air Case 2.

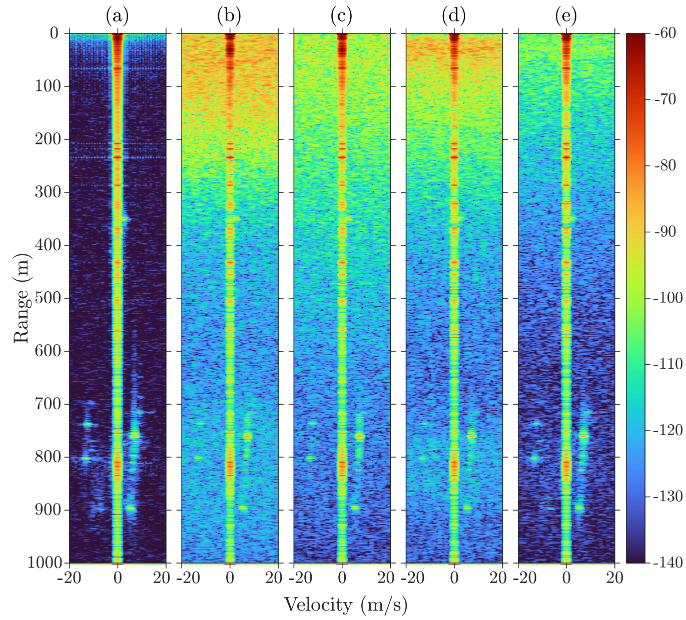

Fig. 20. Range-velocity maps of open-air data (in dB) for: (a) Case 3 (LFM-only) - Matched filtering, (b) Case 1 - Matched Filtering, (c) Case 1 - Mismatched Filtering, (d) Case 2 - Matched Filtering, and (e) Case 2 - Mismatched Filtering. All cases are using a -60 dB Taylor Doppler taper to suppress Doppler sidelobes.

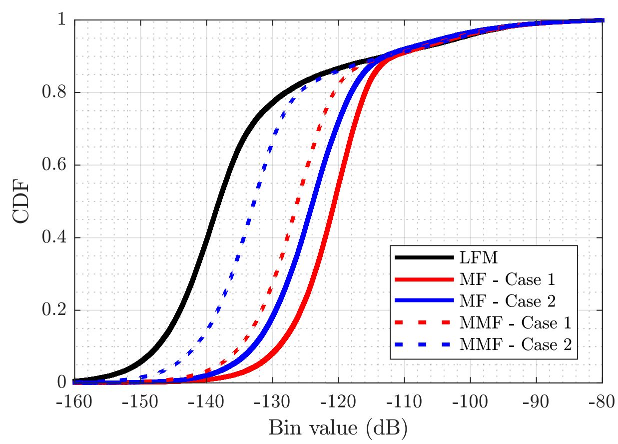

Fig. 21. Cumulative distribution functions of range-velocity maps between 650 and 950 meters and ± 20 m/s for: Case 3 (LFM-only) (black), Case 1 processed using matched filtering (solid red), Case 2 processed using matched filtering (solid blue), Case 1 processed using mismatched filtering (dashed red), and Case 2 processed using mismatched filtering (dashed blue).

a steady state of the CPM phase function at the third symbol, resulting in a shifting up of the phase trajectory after the guard symbols. While they do not typically carry information, these symbols were demodulated as if they carried information and resulted in zero bit errors.

Figure 19 shows a zoomed-in image of the phase trajectories for ideal and open-air signals for each case. These images are similar to the eye-diagrams used in linear modulated communications to demonstrate the quality of the received signal; however, the diagrams presented here are in degrees instead of voltage. Figures 19(a,b) show the zoomed-in unwrapped phase function of the ideal and open-air signals for Case 1, respectively. The high SNR line-of-sight path of the open-air data produces a tight phase response similar to the ideal phase response. Figures 19(c,d) show the zoomed-in unwrapped phase function of the ideal and open-air signals for Case 2, respectively. The reduced phase deflection of Case 2 vs Case 1 (i.e., $h = \frac{1}{8}$ vs $h = \frac{1}{2}$) results in a "noisier" phase response; however, the phase trajectory pattern is still visible, resulting in error-free symbol demodulation via the Viterbi algorithm.

2) Radar Results: The CPIs for each case were also captured at the radar receiver and post-processed using the matched and mismatched filters designed using the loopback captured pulses as discussed in Section V-A. The difference between the processed CPIs is minimal; therefore, we evaluate one of the many CPIs captured during testing to highlight the radar performance.

Figure 20 shows the processed range-velocity maps (in dB) for ranges 0 to 1,000 m and velocities ± 20 m/s for all transmission cases and pulse compression filters. A -60 dB Taylor taper is used in all images to lower the Doppler sidelobes. The scene consists of a large direct-path leakage component near zero range and velocity, a clutter ridge located at zero-velocity, and multiple targets-of-opportunity between 650 and 950 m. As a baseline for performance, Fig. 20(a) shows the Case 3 (i.e., LFM-only) range-velocity map processed using matched filtering for range compression. The Case 1 range-velocity maps for matched and mismatched range compression are shown in Figs. 20(b,c), respectively. The Case 2 range-velocity maps for matched and mismatched filter range compression are shown in Figs. 20(d,e), respectively. Qualitatively, Case 1 with matched filtering results in the largest RSM response (most degradation). Furthermore, both mismatched filter cases are effective in reducing the C-RSM power relative to their corresponding matched filter range-velocity maps. Unsurprisingly, the LFM-only Case 3 has the best overall radar performance since it experiences no RSM.

To quantify the radar performance of each range-velocity map, a cumulative distribution function (CDF) is generated for each case that reveals the floor of the range-Doppler map and

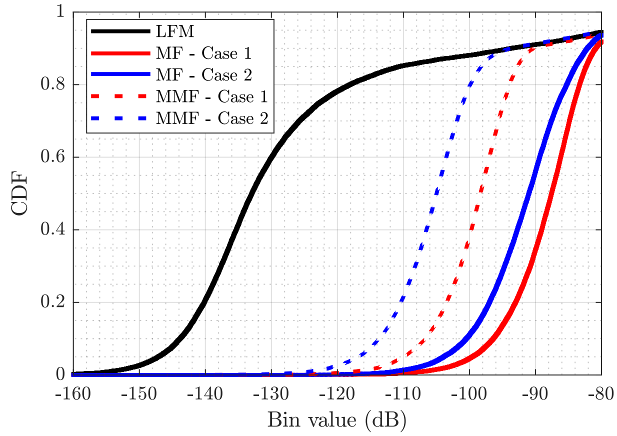

Fig. 22. Cumulative distribution functions of range-velocity maps between 0 and 100 meters and ± 20 m/s for: Case 3 (LFM-only) (black), Case 1 processed using matched filtering (solid red), Case 2 processed using matched filtering (solid blue), Case 1 processed using mismatched filtering (dashed red), and Case 2 processed using mismatched filtering (dashed blue).

demonstrates the reduction of C-RSM power in the image. The CDF of the range-Doppler map is analyzed as the level of the noise and/or RSM floor directly translates to detectability of a target. Figure 21 shows the CDF of each image in Fig. 20 for the region where the targets-of-opportunity reside (i.e., ranges 650 to 950 m and velocities ± 20 m/s). The clutter and targets are located at the higher CDF bin values, and the background floor of the range-velocity map is located in the lower CDF bin values. The offset between the CDF curves at lower bins values quantifies the quality of the images since the separation between the target peaks and the background floor directly relates to probability of target detection. The difference in median bin values (i.e., bin values at CDF of 0.5) is used to determine the suppression of RSM due to mismatched filtering. The reduction in C-RSM power due to mismatched filter is 5.6 dB for Case 1 and 9.2 dB for Case 2, and the C-RSM power for Case 2 mismatched filtering is 5.1 dB above Case 3 (LFM-only). These C-RSM reductions are not what was expected from the analysis in Section V-A because the C-RSM power in this region is largely due to the RSM produced by the direct-path leakage that (for $T = 10$ μs) extends to (at least) $1,500$ m. To see the expected mismatched filtering benefit of 11 and 15 dB for Cases 1 and 2, respectively, Fig. 22 shows the CDF for the region that contains the direct path leakage (i.e., ranges 0 to 100 m and ± 20 m/s). Note, however, that the separation between the LFM and PARC CDFs is much larger for this region due to the high SNR direct-path leakage resulting in an increased C-RSM. While the application of mismatched filters for range compression have mitigated C-RSM to a large degree, the resulting radar performance may not be sufficient given system requirements. To further mitigate the C-RSM beyond what was demonstrated here one must either reduce the modulation index or symbol rate of the communications component (i.e., trade-off communications performance), or accept more SNR loss in the mismatched filter design.

VI. Summary and Future Directions

We have introduced a CPM-based phase-attached radar-communications (PARC) waveform whereby a common base radar phase function is combined with a CPM communications phase function to produce a constant-amplitude and continuous-phase waveform model. The stochastic nature of the embedded communications produces a pulse-agile transmission where the autocorrelation sidelobes of each pulse are modulated by the symbol sequence. The resulting C-RSM produced by these modulating sidelobes spreads clutter energy over the entire Doppler space, which can mask targets of interest (thus degrading radar performance). The severity of C-RSM is directly tied to the communications parameters (i.e., modulation order, modulation index, symbol rate, and shaping filter), and therefore can be tuned to reduce RSM at the expense of communication performance (e.g., higher BER or lower data throughput). Under the assumption of homogeneous clutter statistics, we introduced a method of predicting the expected C-RSM power given a set of PARC waveform parameters and method of fast-time (pulse compression) and slow-time (Doppler compression) processing. To make the radar-communications trade-space more advantageous for each function, we designed mismatched filters to match the cross-correlation response of each pulse to the expected autocorrelation response over the set of all symbol sequences, which largely decouples fast-time and slow-time by reducing RSM (and C-RSM). Finally, the CPM-based PARC waveform was experimentally validated in an open-air environment with a quasi-monostatic radar configuration and communications receiver.

The tunability of the CPM-based PARC framework provides a means to control the performance the radar and communications functions allowing for a flexible co-designed DFRC implementation. This demonstration of spectrum sharing is an initial foray into the capabilities of the PARC signal structure. Additional research problems still need investigating to maximally leverage the flexibility of PARC. For instance, the selection of PARC parameters is a crucial decision in the radar and communications performance trade-space. Joint-optimality of each function could be achieved by defining a quantifiable objective based on prioritization of each function. Furthermore, this work only considers a simple synchronization at the communications receiver, where dispersive channel effects (both time and Doppler) require equalization methods. Because the PARC waveform will likely have (relatively) high bandwidth, the channel response will likely be frequency-selective. Methods to perform equalization in conjunction with removal of the base radar phase function will be considered in future works.

Appendix – Derivation of (23)

Define the peak-normalized Doppler PSD due to clutter as the ratio of the Doppler PSD due to clutter normalized by the response at $f_{\text{D}} = 0$,

$$P_{\text{C}}(f_{\text{D}}) = \frac{\mathcal{E}_{\mathbf{c}}\{|(\mathbf{t} \odot \mathbf{a}(f_{\text{D}}))^H \mathbf{c}|^2\}}{\mathcal{E}_{\mathbf{c}}\{|(\mathbf{t} \odot \mathbf{a}(0))^H \mathbf{c}|^2\}}.$$

Expanding the expected Doppler PSD due to clutter yields

$$\mathcal{E}_{\mathbf{c}}\{|(\mathbf{t} \odot \mathbf{a}(f_{\text{D}}))^H \mathbf{c}|^2\} = (\mathbf{t} \odot \mathbf{a}(f_{\text{D}}))^H \mathcal{E}_{\mathbf{c}}\{\mathbf{c}\mathbf{c}^H\}(\mathbf{t} \odot \mathbf{a}(f_{\text{D}})),$$

where
$$\mathcal{E}_{\mathbf{c}}\{\mathbf{c}\mathbf{c}^H\} = \mathcal{E}_{\mathbf{x}}\{\bar{\mathbf{R}}^T\mathbf{x}\mathbf{x}^H\bar{\mathbf{R}}^*\}$$
$$= \bar{\mathbf{R}}^T\mathcal{E}_{\mathbf{x}}\{\mathbf{x}\mathbf{x}^H\}\bar{\mathbf{R}}^*,$$

and $\mathcal{E}_{\mathbf{x}}\{\bullet\}$ is the expected value over $\mathbf{x}$. We have defined $\mathbf{x}$ as a zero-mean, white, complex-valued Gaussian random vector with variance σ_{x}^2; therefore, $\mathcal{E}_{\mathbf{x}}\{\mathbf{x}\mathbf{x}^H\} = \sigma_x^2\mathbf{I}$ for identity matrix $\mathbf{I}$. Therefore,

$$\mathcal{E}_{\mathbf{c}}\{\mathbf{c}\mathbf{c}^H\} = \sigma_{\mathrm{x}}^2\bar{\mathbf{R}}^T\bar{\mathbf{R}}^*.$$

Noting that $\mathbf{a}(0) = \mathbf{1}$ is a vector of ones, it follows that,

$$P_{\mathrm{C}}(f_{\mathrm{D}}) = \frac{(\mathbf{t}\odot\mathbf{a}(f_{\mathrm{D}}))^H\bar{\mathbf{R}}^T\bar{\mathbf{R}}^*(\mathbf{t}\odot\mathbf{a}(f_{\mathrm{D}}))}{\mathbf{t}^H\bar{\mathbf{R}}^T\bar{\mathbf{R}}^*\mathbf{t}}.$$

References

[1] H. Griffiths, L. Cohen, S. Watts, E. Mokole, C. Baker, M. Wicks, and S. D. Blunt, "Radar spectrum engineering and management: technical and regulatory issues," *Proceedings of the IEEE*, vol. 103, pp. 85–102, Jan. 2015.

[2] J. G. Andrews, S. Buzzi, W. Choi, S. V. Hanly, A. Lozano, A. C. K. Soong, and J. C. Zhang, "What will 5g be?," *IEEE Journal on Selected Areas in Communications*, vol. 32, pp. 1065–1082, June 2014.

[3] B. Paul, A. R. Chiriyath, and D. W. Bliss, "Survey of RF communications and sensing convergence research," *IEEE Access*, vol. 5, pp. 252–270, 2017.

[4] I. F. Akyildiz, W.-Y. Lee, M. C. Vuran, and S. Mohanty, "NeXt generation/dynamic spectrum access/cognitive radio wireless networks: a survey," *Computer Networks*, vol. 50, pp. 2127–2159, Sep. 2006.

[5] Strategic Technology Office and Defense Advanced Research Projects Agency, *Shared spectrum access for radar and communications (SSPARC)*. [Online]. Available: http://www.darpa.mil/program/shared-spectrum-access-for-radar-and-communications, accessed May 2018.

[6] B. H. Kirk, R. M. Narayanan, K. A. Gallagher, A. F. Martone, and K. D. Sherbondy, "Avoidance of time-varying radio frequency interference with software-defined cognitive radar," *IEEE Transactions on Aerospace and Electronic Systems*, vol. 55, no. 3, pp. 1090–1107, 2019.

[7] J. Owen, C. Mohr, B. Ravenscroft, S. Blunt, B. Kirk, and A. Martone, "Real-time experimental demonstration and evaluation of open-air sense-and-notch radar," in *2022 IEEE Radar Conference (RadarConf22)*, pp. 1–6, 2022.

[8] R. G. Mattingly and J. G. Metcalf, "Fast adaptive spectrum sensing using hardware optimized, cell averaging estimation for cognitive radio and radar applications," *IEEE Transactions on Aerospace and Electronic Systems*, vol. 59, no. 5, pp. 5084–5096, 2023.

[9] L. Zheng, M. Lops, Y. C. Eldar, and X. Wang, "Radar and communication coexistence: An overview: A review of recent methods," *IEEE Signal Processing Magazine*, vol. 36, no. 5, pp. 85–99, 2019.

[10] J. A. Zhang, F. Liu, C. Masouros, R. W. Heath, Z. Feng, L. Zheng, and A. Petropulu, "An overview of signal processing techniques for joint communication and radar sensing," *IEEE Journal of Selected Topics in Signal Processing*, vol. 15, no. 6, pp. 1295–1315, 2021.

[11] W. Zhou, R. Zhang, G. Chen, and W. Wu, "Integrated sensing and communication waveform design: A survey," *IEEE Open Journal of the Communications Society*, vol. 3, pp. 1930–1949, 2022.

[12] M. Piezzo, A. De Maio, A. Aubry, and A. Farina, "Cognitive radar waveform design for spectral coexistence," in *2013 IEEE Radar Conference (RadarCon13)*, pp. 1–4, 2013.

[13] A. Aubry, A. De Maio, Y. Huang, M. Piezzo, and A. Farina, "A new radar waveform design algorithm with improved feasibility for spectral coexistence," *IEEE Transactions on Aerospace and Electronic Systems*, vol. 51, no. 2, pp. 1029–1038, 2015.

[14] A. Aubry, V. Carotenuto, and A. D. Maio, "Forcing multiple spectral compatibility constraints in radar waveforms," *IEEE Signal Processing Letters*, vol. 23, no. 4, pp. 483–487, 2016.

[15] B. Ravenscroft, J. W. Owen, J. Jakabosky, S. D. Blunt, A. F. Martone, and K. D. Sherbondy, "Experimental demonstration and analysis of cognitive spectrum sensing and notching for radar," *IET Radar, Sonar & Navigation*, vol. 12, no. 12, pp. 1466–1475, 2018.

[16] C. A. Mohr and S. D. Blunt, "Analytical spectrum representation for physical waveform optimization requiring extreme fidelity," in *2019 IEEE Radar Conference (RadarConf)*, pp. 1–6, 2019.

[17] A. Hassanien, M. G. Amin, E. Aboutanios, and B. Himed, "Dual-function radar communication systems: A solution to the spectrum congestion problem," *IEEE Signal Processing Magazine*, vol. 36, no. 5, pp. 115–126, 2019.

[18] F. Liu, C. Masouros, A. P. Petropulu, H. Griffiths, and L. Hanzo, "Joint radar and communication design: Applications, state-of-the-art, and the road ahead," *IEEE Transactions on Communications*, vol. 68, no. 6, pp. 3834–3862, 2020.

[19] T. M. Cover and J. A. Thomas, *Elements of Information Theory*. Hoboken, NJ: John Wiley & Sons, 2006.

[20] M. A. Richards, *Fundamentals of Radar Signal Processing*. New York City, NY: McGraw-Hill Education, 2014.

[21] M. Wicks, E. Mokole, S. Blunt, R. Schneible, and V. Amuso, eds., *Principles of Waveform Diversity and Design*. Raleigh, NC: SciTech Publishing, 2010.

[22] S. Pillai, K. Y. Li, and B. Himed, *Waveform Diversity: Theory & Applications*. New York, NY: McGraw-Hill, 2011.

[23] F. Gini, A. D. Maio, and L. K. Patton, eds., *Waveform Design and Diversity for Advanced Radar Systems*. Croydon, UK: Institution of Engineering and Technology, 2012.

[24] S. D. Blunt and E. L. Mokole, "Overview of radar waveform diversity," *IEEE Aerospace and Electronic Systems Magazine*, vol. 31, pp. 2–42, Nov. 2016.

[25] S. Blunt and E. S. Perrins, eds., *Radar & Communications Spectrum Sharing*. London, United Kingdom: IET, 2018.

[26] S. D. Blunt, M. R. Cook, and J. Stiles, "Embedding information into radar emissions via waveform implementation," *International Waveform Diversity and Design Conference*, pp. 195–199, Niagara Falls, Canada, Aug. 2010.

[27] A. C. O'Connor, J. M. Kantor, and J. Jakabosky, "Joint equalization filters that mitigate waveform-diversity modulation of clutter," *IEEE Radar Conference*, Philadelphia, PA, May 2016.

[28] A. Hassanien, M. G. Amin, Y. D. Zhang, and F. Ahmad, "Dual-function radar-communications: information embedding using sidelobe control and waveform diversity," *IEEE Transactions on Signal Processing*, vol. 64, pp. 2168–2181, Apr. 2016.

[29] C. Sturm and W. Wiesbeck, "Waveform design and signal processing aspects for fusion of wireless communications and radar sensing," *Proceedings of the IEEE*, vol. 99, pp. 1236–1259, July 2011.

[30] B. Ravenscroft, P. M. McCormick, S. D. Blunt, E. Perrins, and J. G. Metcalf, "A power-efficient formulation of tandem-hopped radar & communications," *IEEE Radar Conference*, Oklahoma City, OK Apr. 2018.

[31] M. Roberton and E. R. Brown, "Integrated radar and communications based on chirped spread-spectrum techniques," *IEEE/MTT-S International Microwave Symposium*, pp. 611.–614, Philadelphia, PA, June, 2003.

[32] X. Chen, X. Wang, S. Xu, and J. Zhang, "A novel radar waveform compatible with communication," *International Conference on Computational Problem-Solving*, pp. 177–181, Chengdu, China, Oct. 2011.

[33] M. Nowak, M. Wicks, Z. Zhang, and Z. Wu, "Co-designed radar-communication using linear frequency modulation waveform," *IEEE Aerospace and Electronic Systems Magazine*, vol. 31, pp. 28–35, Oct. 2016.

[34] F. Liu, Y. Cui, C. Masouros, J. Xu, T. X. Han, Y. C. Eldar, and S. Buzzi, "Integrated sensing and communications: Toward dual-functional wireless networks for 6g and beyond," *IEEE Journal on Selected Areas in Communications*, vol. 40, no. 6, pp. 1728–1767, 2022.

[35] Range Commanders Council Telemetry Group, Range Commanders Council, White Sands Missile Range, New Mexico, *IRIG Standard 106-04: Telemetry Standards*, 2004. (Available online at http://www.ntia.doc.gov/osmhome/106.pdf).

[36] J. B. Anderson, T. Aulin, and C.-E. Sundberg, *Digital Phase Modulation*. New York, NY: Plenum Press, 1986.

[37] Bluetooth Special Interest Group, "Specifications of the Bluetooth System, Version 1.2," November 2003.

[38] D. I. S. Agency, "Department of Defense interface standard, interoperability standard for single-access 5-kHz and 25-kHz UHF satellite communications channels." Tech. Rep. MIL-STD-188-181B, Department of Defense, March 1999.

[39] J. Jakabosky, S. D. Blunt, and B. Himed, "Spectral-shape optimized FM noise radar for pulse agility," *IEEE Radar Conference*, Philadelphia, PA, May 2016.

[40] C. Sahin, J. G. Metcalf, and S. D. Blunt, "Characterization of range sidelobe modulation arising from radar embedded-communications," *IET International Conference on Radar Systems*, Belfast, UK, Oct. 2017.

[41] C. Sahin, J. Jakabosky, P. M. McCormick, J. G. Metcalf, and S. D. Blunt, “A novel approach for embedding communication symbols into physical radar waveforms,” *IEEE Radar Conference*, pp. 1498–1503, Seattle, WA, May 2017.

[42] J. G. Proakis, *Digital Communications*. New York, NY: McGraw-Hill Education, 2008.

[43] C. Sahin, J. G. Metcalf, and S. D. Blunt, “Filter design to address range sidelobe modulation in transmit-encoded radar-embedded communications,” *IEEE Radar Conference*, pp. 1509–1514, Seattle, WA, May 2017.

[44] M.-E. Chatzitheodoridi, A. Taylor, O. Rabaste, and H. Oriot, “A cooperative sar-communication system using continuous phase modulation codes and mismatched filters,” *IEEE Transactions on Geoscience and Remote Sensing*, vol. 61, pp. 1–14, 2023.

[45] C. Sahin, J. G. Metcalf, A. Kordik, T. Kendo, and T. Corigliano, “Experimental validation of phase-attached radar/communications: Radar performance,” *International Conference on Radar*, Brisbane, Australia, Aug. 2018.

[46] S. D. Blunt, J. K. Jakabosky, C. A. Mohr, P. M. McCormick, J. W. Owen, B. Ravenscroft, C. Sahin, G. D. Zook, C. C. Jones, J. G. Metcalf, and T. Higgins, “Principles and applications of random fm radar waveform design,” *IEEE Aerospace and Electronic Systems Magazine*, vol. 35, no. 10, pp. 20–28, 2020.

[47] A. W. Doerry, “Generating nonlinear FM chirp waveforms for radar,” No. SAND2006-5856. Sandia National Laboratories (SNL), Albuquerque, NM, and Livermore, CA (United States), 2006.

[48] M. Simon, *Bandwidth-Efficient Digital Modulation With Application to Deep-Space Communication*. New York, NY: Wiley, 2003.

[49] U. Mengali, *Synchronization techniques for digital receivers*. Springer Science & Business Media, 2013.

[50] A. Viterbi, “Error bounds for convolutional codes and an asymptotically optimum decoding algorithm,” *IEEE Transactions on Information Theory*, vol. 13, pp. 260–269, Apr. 1967.

[51] T. Higgins, K. Gerlach, A. K. Shackelford, and S. D. Blunt, “Aspects of non-identical multiple pulse compression,” *IEEE Radar Conference*, pp. 895–900, Kansas City, MO, May 2011.

[52] D. Scholnik, “Range-ambigious clutter suppression with pulse-diverse waveforms,” *IEEE Radar Conference*, pp. 336–341, Kansas City, MO, May 2011.

[53] C. Sahin, J. G. Metcalf, and B. Himed, “Reduced complexity maximum SINR receiver processing for transmit-encoded radar-embedded communications,” *IEEE Radar Conference*, Oklahoma City, OK, Apr. 2018.

[54] C. Jones, B. Ravenscroft, J. Vogel, S. M. Shontz, T. Higgins, K. Wagner, and S. Blunt, “Computationally efficient joint-domain clutter cancellation for waveform-agile radar,” *IEEE Radar Conference*, Atlanta, GA, May 2021.

[55] M. H. Ackroyd and F. Ghani, “Optimum mismatched filters for sidelobe suppression,” *IEEE Transactions on Aerospace and Electronic Systems*, vol. AES-9, pp. 214–218, Mar. 1973.

[56] C. C. Jones, P. M. McCormick, and M. B. Heintzelman, “Computationally efficient constraint-optimized radar mismatched filtering for waveform-agile systems,” *IEEE Transactions on Aerospace and Electronic Systems*, pp. 1–23, 2025.

[57] X. He, L. Hu, Z. Wu, and null Shunjun Wu, *Optimal sidelobe suppression filters design with a constraint of maximum loss in process gain*, p. 381.

[58] O. Rabaste and L. Savy, “Mismatched filter optimization for radar applications using quadratically constrained quadratic programs,” *IEEE Transactions on Aerospace and Electronic Systems*, vol. 51, no. 4, pp. 3107–3122, 2015.

[59] T. Aittomäki and V. Koivunen, “Mismatched filter design and interference mitigation for mimo radars,” *IEEE Transactions on Signal Processing*, vol. 65, no. 2, pp. 454–466, 2017.

[60] M. A. Richards, J. A. Scheer, and W. Holm, *Principles of Modern Radar, Vol. I: Basic Principles*. Raleigh, NC: SciTech Publishing, 2010.

[61] T. Higgins, S. D. Blunt, and A. K. Shackelford, “Time-range adaptive processing for pulse agile radar,” *International Waveform Diversity and Design Conference*, pp. 115–120, Niagara Falls, Canada, Aug. 2011.

[62] S. Boyd and L. Vandenberghe, *Convex optimization*. Cambridge university press, 2004.

Cenk Sahin (S’06–M’16) received his B.S. degree in electrical and computer engineering from the University of Missouri – Kansas City, MO in 2008, and his M.S. and Ph.D. degrees both in electrical engineering, from the University of Kansas, Lawrence, KS, in 2012 and 2015, respectively. He received the Richard K. & Wilma S. Moore PhD Dissertation Award given to the best PhD dissertation in the Department of Electrical Engineering & Computer Science, University of Kansas. For his PhD work he characterized channel coding and latency performance of various practical modulation schemes over wireless fading channels. In 2016 Cenk Sahin was awarded the National Research Council (NRC) Postdoctoral Research Fellowship. As an NRC fellow at AFRL (2016-2018) he developed a family of spectrally-efficient constant-modulus radar-embedded communications waveforms. From 2018 to 2023 he was with the RF Technology Branch at the Sensors Directorate, Air Force Research Laboratory, WPAFB, OH where he led the design, development, and testing of spectrum-sharing methods for radar and communications, radar-embedded communication waveforms, and signal processing techniques for dual-function systems. Since May 2023 Dr. Cenk Sahin has been with the Sensors Technologies Group, Air and Missile Defense Sector, Johns Hopkins University (JHU) Applied Physics Laboratory (APL). He is the author of 7 journal papers, 5 (1 issued, 4 pending) patents, 23 peer-reviewed conference papers and 2 book chapters.

Patrick M McCormick (S’12–M’18) received his B.S. degree in mechanical engineering, B.S. in electrical engineering, and Ph.D. degree in electrical engineering from the University of Kansas, Lawrence, KS, USA, in 2008, 2013, and 2018, respectively. From 2018 to 2021, he served as a research electronics engineer with the Air Force Research Laboratory - Sensors Directorate, Wright-Patterson AFB, OH. In 2021, he began his current position as an Assistant Professor at the University of Kansas in the Electrical Engineering and Computer Science department. He has multiple refereed journal publications, conference papers, book chapters, and patents in the areas of waveform diversity and design, adaptive receive signal processing, and radar/communication spectrum sharing. Dr. McCormick was awarded the 2018 IEEE AESS Robert T. Hill Best Dissertation Award for his work in radar waveform design and optimization and is a 2023 DARPA Young Faculty Award recipient. He has been an Associate Editor for IEEE Transactions on Aerospace and Electronic Systems since 2024 and has been a member of the IEEE AESS Radar Systems Panel since 2023.

Justin G. Metcalf (S'08–M'15–SM'19) received the bachelor's degree in computer engineering from Kansas State University, Manhattan, KS, USA, in 2006, and the master's and Ph.D. degrees in electrical engineering from the University of Kansas, Lawrence, KS, USA, in 2011 and 2015, respectively. From 2006 to 2008, he was with Flight Simulation Laboratories, Lockheed Martin Aeronautics, Fort Worth, TX, USA. From 2008 to 2014, he was with the Radar Systems Laboratory, University of Kansas. From 2014 to 2018, he was a Research Electronics Engineer with the Sensors Directorate of the Air Force Research Laboratory, Wright-Patterson AFB, OH, USA. He has been with the School of Electrical and Computer Engineering, The University of Oklahoma, Norman, OK, USA, where he is also a member of the Advanced Radar Research Center, as an Assistant Professor (2018-2024) and Associate Professor (2025-Present). Dr. Metcalf has been a member of the IEEE AESS Radar Systems Panel since 2020. He was a recipient of the Richard and Wilma Moore Award for the Best Departmental Master's Thesis from 2011 to 2012, the 2017 IEEE Dayton Section Young Professionals Award, the 2020 DARPA Young Faculty Award, and the 2023 IEEE AESS Fred Nathanson Memorial Radar Award. He was the Chair of the Dayton Chapter of the IEEE Aerospace and Electronic Systems Society from 2016 to 2018 and the General Co-Chair of the 2024 IEEE Radar Conference in Denver, Colorado. At the he University of Oklahoma he was an Aerospace and Defense Faculty Fellow from 2023-2024 and the Associate Director of Spectrum Dominance for the Oklahoma Aerospace and Defense Institute (OADII) since 2024. He has been an Associate Editor of IEEE Transactions on Aerospace and Electronic Systems since 2023.

John Jakabosky received a B.S. degree in electrical engineering in 2010 and a M.Eng degree in Electrical Engineering and Computer Science in 2022, both from the University of Kansas. Since 2016 he has worked as an Electronics Engineer at the Naval Research Laboratory, Washington, D.C., USA. His research interests include waveform diversity, radar signal processing, and radar hardware design.

Shannon D. Blunt (S'96–M'02–SM'07–F'16) is the Roy A. Roberts Distinguished Professor of Electrical Engineering & Computer Science (EECS) at the University of Kansas (KU), Director of the KU Radar Systems & Remote Sensing Lab (RSL), and Director of the Kansas Applied Research Lab (KARL). He received a PhD in electrical engineering from the University of Missouri in 2002, and from 2002 until 2005 he was with the Radar Division of the U.S. Naval Research Laboratory in Washington, D.C. He received an AFOSR Young Investigator Award in 2008, the IEEE/AESS Nathanson Memorial Radar Award in 2012, was named a Fellow of the IEEE in 2016, was appointed to the U.S. President's Council of Advisors on Science & Technology (PCAST) in 2019, received the 2020 IET Radar, Sonar & Navigation Premium Award, and was named a Fellow of the Military Sensing Symposia (MSS) in 2024, along with multiple teaching awards. He has over 200 refereed journal, conference, and book chapter publications, and 19 patents/patents-pending. He co-edited the books Principles of Waveform Diversity & Design (2010) and Radar & Communication Spectrum Sharing (2018).

He has served as a subject matter expert on radar spectrum for DARPA, the Air Force's S&T 2030 Initiative, the National Spectrum Consortium, the Office of the Under Secretary of Defense for Research & Engineering (OUSD(R&E)), and the White House Office of Science & Technology Policy (OSTP). He served as Chair of the IEEE/AESS Radar Systems Panel and on the AESS Board of Governors. He is Editor-in-Chief for IEEE Transactions on Radar Systems, served on the Editorial Board for IET Radar, Sonar & Navigation, and served in different editorial roles for IEEE Transactions on Aerospace & Electronic Systems. He has been General Chair or Technical Chair for multiple IEEE Radar Conferences and serves on the Program Committee for the MSS Tri-Service Radar Symposium series. He was also Chair of the NATO SET-179 research task group on "Dynamic Waveform Diversity & Design".

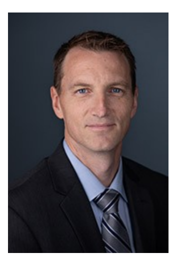

Erik Perrins (S'96–M'05–SM'06) received the B.S. (*magna cum laude*), M.S., and Ph.D. degrees from BYU, Provo, UT, in 1997, 1998, and 2005, respectively all in electrical engineering. From 1998 to 2004, he was with Motorola, Inc., Schaumburg, IL, where he was engaged in research on land mobile radio products. Since August 2005, he has been with the Department of Electrical Engineering and Computer Science, University of Kansas, Lawrence, where he is currently a University Distinguished Professor and Department Chair. Since 2004, he has also been an industry consultant on problems such as reduced-complexity receiver design, receiver synchronization, and error control coding. His current research interests include digital communication theory, synchronization, channel coding, energy efficient communications, and complexity reduction in receivers.

Dr. Perrins is a member of the IEEE Aerospace & Electronic Systems Society and the IEEE Communications Society. He was an Editor and an Area Editor for the IEEE TRANSACTIONS ON COMMUNICATIONS from 2007–2018, and was the Chair of the Communication Theory Technical Committee within the IEEE Communications Society from 2017–2018.

Jonathan Owen (S'16, M'23) received his Ph.D. E.E. degree in 2023. He is currently an Assistant Research Professor affiliated with the Radar Systems Laboratory (RSL) at the University of Kansas. He collaborated with the Sensors and Electronic Devices Directorate (SEDD) of the Army Research Laboratory (ARL) from 2016 to 2020, pushing forward research and development of real-time radar spectrum sharing capabilities while garnering expertise in field-programmable gate array (FPGA) technology. For efforts advancing spectrum sharing radar, he received publication awards including the 2018 IET Radar, Sonar and Navigation Premium Award, 1st Place in the 2022 IEEE Radar Conference Student Paper Competition, and 3rd Place in the 2019 ARL Student Competition. He interned at MIT Lincoln Laboratory in 2021, implementing radar signal processing algorithms on GPU for real-time performance. With a variety of publications in waveform diversity, radar signal processing, and real-time implementation of non-traditional algorithms, he contributes a modern knowledge about prototyping of practical radar systems.